

# Coupled Atomic Wires in a Synthetic Magnetic Field

J. C. Budich<sup>1</sup>, A. Elben<sup>2,3</sup>, M. Łański<sup>2,3</sup>, A. Sterdyniak<sup>4</sup>, M. A. Baranov<sup>2,3</sup>, P. Zoller<sup>2,3,4</sup>

<sup>(1)</sup> *Department of Physics, University of Gothenburg, SE 412 96 Gothenburg, Sweden*

<sup>(2)</sup> *Institute for Theoretical Physics, University of Innsbruck, A-6020 Innsbruck, Austria*

<sup>(3)</sup> *Institute for Quantum Optics and Quantum Information of the Austrian Academy of Sciences, A-6020 Innsbruck, Austria and*

<sup>(4)</sup> *Max-Planck-Institute of Quantum Optics, Hans-Kopfermann-Str. 1, D-85748 Garching, Germany*

(Dated: March 11, 2022)

We propose and study systems of coupled atomic wires in a perpendicular synthetic magnetic field as a platform to realize exotic phases of quantum matter. This includes (fractional) quantum Hall states in arrays of many wires inspired by the pioneering work [Kane et al. PRL **88**, 036401 (2002)], as well as Meissner phases and Vortex phases in double-wires. With one continuous and one discrete spatial dimension, the proposed setup naturally complements recently realized discrete counterparts, i.e. the Harper-Hofstadter model and the two leg flux ladder, respectively. We present both an in-depth theoretical study and a detailed experimental proposal to make the unique properties of the *semi-continuous Harper-Hofstadter model* accessible with cold atom experiments. For the minimal setup of a double-wire, we explore how a sub-wavelength spacing of the wires can be implemented. This construction increases the relevant energy scales by at least an order of magnitude compared to ordinary optical lattices, thus rendering subtle many-body phenomena such as Lifshitz transitions in Fermi gases observable in an experimentally realistic parameter regime. For arrays of many wires, we discuss the emergence of Chern bands with readily tunable flatness of the dispersion and show how fractional quantum Hall states can be stabilized in such systems. Using for the creation of optical potentials Laguerre-Gauss beams that carry orbital angular momentum, we detail how the coupled atomic wire setups can be realized in non-planar geometries such as cylinders, discs, and tori.

## I. INTRODUCTION

Synthetic matter based on ultracold atomic gases in optical potentials [1] has established itself as one of the most promising experimental routes to realize exotic quantum matter [2, 3]. Recent theoretical [4–10] and seminal experimental [11–16] results on the implementation of synthetic magnetic fields and even non-Abelian gauge fields such as synthetic spin-orbit coupling [17] have paved the way towards realizing topological insulators [18, 19] with ultracold atoms [3]. In particular, the Harper Hofstadter (HH) Hamiltonian [20], introduced to describe the motion of electrons in a 2D square lattice exposed to a perpendicular magnetic field has recently been experimentally realized with cold atoms in optical lattices [13, 14].

In the present work, we propose and present a detailed study of ultracold atomic gases confined to an array of coupled wires forming a 2D system with *one continuous and one discrete dimension* with synthetic magnetic fields. Employing Raman-assisted tunneling techniques [4, 6, 8] to generate artificial magnetic fluxes, we introduce an experimentally feasible scheme for the implementation of a semi-continuous generalization of the HH model. We are interested in particular in a physical realization of this model for various geometries: this includes a planar setup (see Fig. 1(a)), which can be realized as a variant of existing cold atom experiments with optical lattices, or as disks, cylinders, or tori (see Fig. 1 (b)-(c)), which is achieved by employing optical potentials created from Laguerre-Gauss laser beams carrying orbital angular momentum (OAM) [21–23]. Below, we will consider

both bosonic and fermionic atomic quantum many-body systems, and we will explore the rich variety of exotic phases of matter that can be realized in such coupled atomic wires.

The non-interacting part  $H_0$  of the Hamiltonian describing an array of coupled wires is given by

$$H_0 = \sum_y \int dx \left[ \psi_{x,y}^\dagger \frac{p_x^2}{2m} \psi_{x,y} + (J_x \psi_{x,y}^\dagger \psi_{x,y+a} + \text{h.c.}) \right]. \quad (1)$$

Here,  $\psi_{x,y}$  annihilates a particle at position  $\mathbf{r} = (x, y)$ , and  $J_x = J e^{i\phi x}$  ( $J > 0$ ) denotes the complex hopping amplitude in the discrete  $y$ -direction for atoms of mass  $m$ , where  $\phi$  determines the homogeneous synthetic magnetic flux of the system, defining a magnetic length  $l_B \equiv 2\pi/\phi$ , and  $a$  denotes the lattice spacing in  $y$ -direction. We note that for non-planar geometries (see Fig. 1 (b)-(c)), the coordinates  $x, y$  should be understood as local coordinates tangent to the curved 2D system, where  $x$  always represents the continuous (i.e. for coupled rings circumferential) direction, and  $y$  refers to sites in the discrete direction. In the atomic context,  $H_0$  can be realized both with fermionic and bosonic atoms. The long-wavelength scattering between the atoms gives rise to a (two-body) interaction  $H_I$ , and the total Hamiltonian is hence given by

$$H = H_0 + H_I. \quad (2)$$

As the relevant scattering channels differ for bosons and fermions thus giving rise to different forms of  $H_I$ , we will

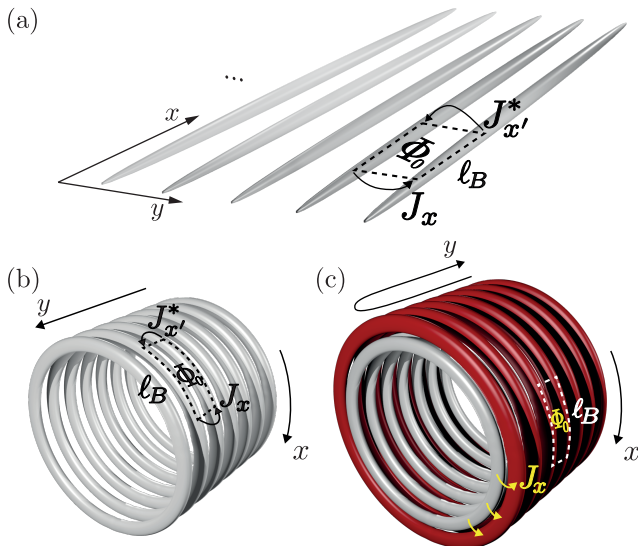


FIG. 1. (Color online) Systems of wires in various geometries coupled by Raman-induced hopping with amplitude  $J_x = J e^{i\phi x}$  inducing artificial magnetic field with a flux quantum  $\Phi_0$  threading a unit cell of length  $l_B$  along the wires. Panel (a) planar geometry. Panel (b) structure of a cylinder spanned by a set of parallel rings. Panel (c) geometry of a torus constructed using two nested coaxial cylinders coupled only at the end rings of each cylinder via Raman-induced hopping.

specify  $H_I$  for the individual examples considered in this work.

In a condensed matter context, similar models have been introduced by Kane et al. [27, 28] for electronic systems to study fractional quantum Hall (FQH) physics [24–26] in tunnel-coupled nano-wires, known as the coupled wire construction. There, the relevance in the renormalization group sense of specific tunnel-coupling terms occurring as perturbations to the strongly correlated uncoupled 1D wires is investigated. Here, we focus on a different limit, where the strongly tunnel-coupled wires form quasi-flat partially filled Chern bands [29] which, adding interactions, host FQH states. Below, we argue how FQH states such as Laughlin states [25] can be stabilized in this setup and present a numerical analysis for realistic parameters in support of these claims. Remarkably, here the flatness of the lowest band can be directly tuned by changing the hopping strength  $J$ . While the controlled realization of coupled wire systems in conventional materials is challenging, the remarkable flexibility and tunability of ultracold atomic gases may open a new playground for the synthetic realization of topological phases of quantum matter.

For a minimal system of *two coupled wires*, we compare for both bosonic and fermionic gases the phase diagram to that of a two-leg ladder – the well studied discrete analog [15, 30–34]. From an experimental point of view, a key challenge is a sufficiently strong couplings  $J$  (with

Raman schemes to realize the artificial gauge field) in relation to the temperature. We will address this problem by proposing a setup of a *double wire with subwavelength separation* extending recent work [35] (see also Ref. [36]), which allows a strong enhancement by Raman-induced tunneling orders of magnitude of the relevant couplings over standard optical lattices schemes with spacing  $a = \lambda/2$ , where  $\lambda$  is the wavelength of the light. In the case of a weakly or non-interacting gas of fermionic atoms, subwavelength double wires promise observation of chiral edge currents with non-analytic behavior for atoms at Lifshitz transitions of the Fermi surface.

The remainder of this paper is structured as follows. In Section II, we theoretically analyze the model of coupled wires, focusing on geometries and parameter regimes that are of immediate relevance for the proposed implementation with ultracold atomic gases that is detailed in Section III. Finally, in Section IV we provide a concluding discussion of our results.

## II. CHERN BANDS AND TOPOLOGICAL PHASES IN COUPLED ATOMIC WIRES

In this Section, we discuss the properties of systems described by the discrete-continuous Hamiltonian with artificial gauge fields given in Eqs. (1) and (2) in various geometries such as planar, cylindrical and toroidal, the experimental implementation of which is discussed in detail in the subsequent Sec. III. In anticipation of the atomic physics analysis, we will identify the relevant physical parameters and energy scales, to be compared with the experimentally achievable parameters for various setups in Sec. III. In Sec. II A, we discuss the topological band structure of the Hamiltonian (1) in the presence of translation invariance, i.e. in the geometry of an infinite plane or a (finite) torus. In Sec. II B, we turn to a cylindrical or planar ribbon geometry of  $N$  wires, and investigate the occurrence of edge states. In Sec. II C, a minimal, analytically treatable case of  $N = 2$  parallel wires or rings is analyzed. Adding interactions, we study in Sec. II D a strongly correlated bosonic gas. In the framework of exact diagonalization, we discuss the realization of robust fractional Quantum Hall physics in flat-band systems.

### A. Translation invariant model

We start by considering the free Hamiltonian in Eq. (1). Assuming translation invariance in  $y$ -direction, we can separate the corresponding motion by using the plane waves with a quasimomentum  $k_y \in [-\pi/a, \pi/a]$  with  $a$  the lattice spacing in the  $y$ -direction. For a given  $k_y$ , the first quantized Hamiltonian in the  $x$ -direction takes the form

$$h_{x,k_y} = -\frac{\hbar^2}{2m} \frac{d^2}{dx^2} + 2J \cos(\phi x + k_y a). \quad (3)$$

Eq. (3) describes a 1D particle moving in a potential with a period given by the magnetic length  $l_B = 2\pi/\phi$ . The corresponding energy scale is given by the magnetic (recoil) energy  $E_R^M \equiv \hbar^2\phi^2/2m$ . The form of Eq. (3) parametrically depends on  $k_y$  in a way that makes the Hall response of the system intuitively clear. Varying  $k_y$  by  $2\pi/a$ , i.e. once around the Brillouin zone (BZ), the potential slides  $\ell_B = 2\pi/\phi$  in  $x$ -direction, i.e. by one period of the potential in Eq. (3). In agreement with this intuitive picture, the Chern number  $\mathcal{C}^\alpha$  of a Bloch band  $\alpha$  [37], defined in terms of the projection  $P_k^\alpha$  onto the Bloch state  $|u_k^\alpha\rangle$  at lattice momentum  $k = (k_x, k_y)$  as

$$\mathcal{C}^\alpha = \frac{i}{2\pi} \int_{BZ} d^2k \operatorname{Tr} \{P_k^\alpha [(\partial_{k_x} P_k^\alpha), (\partial_{k_y} P_k^\alpha)]\} = 1 \quad (4)$$

is always one, irrespective of the parameter values as long as the band is separated by an energy gap from the other bands. As is clear from the translational symmetry of Eq. (3), the spectrum of the system is independent of  $k_y$  and so is the concomitant Berry curvature  $\mathcal{F}_k^\alpha = i\operatorname{Tr} \{P_k^\alpha [(\partial_{k_x} P_k^\alpha), (\partial_{k_y} P_k^\alpha)]\}$ .

An example of the  $k_x$ -dependent band structure is shown in Fig. 2. Interestingly, and in contrast to the discrete HH model, increasing the hopping strength  $J$  here provides a simple knob to make the energy spectrum flat as soon as the dimensionless parameter  $\tilde{J} \equiv J/E_R^M \gtrsim 1$ . The flatness is characterized by the ratio of the gap to the first excited state to the width of the lowest band. For the specific parameters in Fig. 2 we achieve a flatness ratio of 137 already for  $\tilde{J} = 0.8$  (for scaling of the flatness, and of the Berry curvature we refer to Appendix A).

## B. Finite number of wires

We now consider the case of open boundary conditions in the discrete direction, reflecting a finite number  $N$  of infinitely long wires in a planar geometry or  $N$  parallel rings in a cylindrical geometry. In this case,  $k_y$  is not a

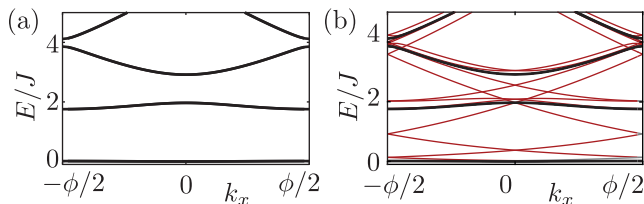


FIG. 2. (Color online) Band structure  $k_x \in [-\phi/2, \phi/2]$  ( $\phi/2 \equiv \pi/\ell_B$ ) of the three lowest bands of the free model Hamiltonian (3). Panel (a) shows a closed geometry of a torus with  $N \gg 1$  wires, or for a planar system with an infinite number of wires. Panel (b) shows energy levels in the limit of  $N \gg 1$  of parallel wires; black lines denote energy levels of states supported in the bulk of the system, red lines show edge states. In both plots, we have chosen  $\tilde{J} \equiv J/(\hbar^2\phi^2/2m) = 0.8$ .

good quantum number. However, each individual wire or ring still possesses  $k_x$ -eigenstates  $|y, k_x\rangle$ , labeled by  $y = y_1, \dots, y_N$ . The eigenvectors of the Hamiltonian (1) are then of the form

$$|\psi\rangle = \sum_{j=1}^N c_j |y_j, k_x + \phi(j - j_0)\rangle, \quad k_x \in [-\phi/2, \phi/2] \quad (5)$$

for some  $j_0 \in \mathbb{Z}$ . For the eigenvectors where the  $c_j$ 's are supported mostly in the bulk of the system, the eigenenergies are similar (for  $N \gg 1$ ) to those for an infinite case. In particular, they are independent of the actual position of the wavefunction in the bulk and feature the same band flatness. Reflecting the unit Chern number of the bands, there are also edge states. For them, the  $|c_j|$  are localized on a few ( $\sim \sqrt[4]{\tilde{J}}$ ) wires, or rings at the boundary and their energies cross the bulk gap between different bands.

Probing such edge modes is possible by inducing a Hall response to a time-dependent magnetic flux along the lines of the Laughlin argument [38]. To that end, in a many-particle system of non-interacting ultracold fermions a synthetic magnetic probe field  $\mathbf{B} = B_0\mathbf{e}_y$  is induced by increasing, in a time-dependent manner, the velocity of the gas in the  $x$  direction. This can be done either by direct stirring [39] or transfer of optical momentum [40]. The result is a measurable transfer of population between edge-modes [41], which allows to verify the topological nature of the Hamiltonian (1).

## C. Minimal setup: Two coupled wires

In this Section, we analyze the minimal setup consisting of only  $N = 2$  coupled wires. It represents the simplest system showing non-trivial artificial magnetic field effects and is readily realized experimentally (see Sec. III) [15, 42, 43]. The physics of many particles in the discrete analog of our system, the two-leg ladder, has been studied intensively theoretically and experimentally [15, 30–34]. For bosonic particles, the two-leg ladder mimics to some extent the behavior of a Type-II superconductor, exhibiting Meissner and vortex phases in a weak and strong external magnetic field, respectively [30, 31, 33]. These phases have been demonstrated experimentally [15]. Here, we find similar phenomena in the bosonic continuous double wire. For fermions, by contrast, we show that no vortex phase is present. Instead, weak and strong field regimes are distinguished by the presence or absence of Lifshitz transitions, respectively, manifesting themselves in non-analyticities of the chiral current.

In the absence of interactions, the physics of the double wire system is governed by the Hamiltonian (1) where the sum in the discrete direction  $y$  is reduced to two wires, labeled with  $L$  (left) and  $R$  (right), respectively. The resulting Hamiltonian (1) can be easily diagonalized in Fourier space for the continuous  $x$ -direction, exhibiting

two energy bands

$$E_{\pm}(k_x) = \frac{\hbar^2 k_x^2}{2m} + \frac{\hbar^2 \phi^2}{2m} \left( \frac{1}{4} \pm \sqrt{\frac{k_x^2}{\phi^2} + \tilde{J}^2} \right). \quad (6)$$

Here,  $\tilde{J} = J/E_R^M$  is the dimensionless interwire coupling introduced above. The wave functions are given by

$$\Psi_{k_x}^{(\pm)}(x) = \left[ 2\sqrt{1 + \left(\frac{k_x}{\tilde{J}\phi}\right)^2} \right]^{-\frac{1}{2}} \begin{pmatrix} f^{\pm\frac{1}{2}} e^{-i\frac{\phi}{2}x} \\ \pm f^{\mp\frac{1}{2}} e^{i\frac{\phi}{2}x} \end{pmatrix} e^{ik_x x} \quad (7)$$

with  $f = \sqrt{1 + (k_x/\tilde{J}\phi)^2} - (k_x/\tilde{J}\phi)$ , where upper (lower) component corresponds to the right  $\Psi_R(x)$  [left  $\Psi_L(x)$ ] wire.

The upper band  $E_+(k_x)$  has in the entire parameter regime a single global minimum at  $k_x = 0$ . The form of the lower band  $E_-(k_x)$  depends on  $\tilde{J}$ . For  $\tilde{J} < 1/2$ , it exhibits two degenerate minima at  $k_x^{(1,2)} = \pm k_g$  with  $k_g = (\phi/2)\sqrt{1 - 4\tilde{J}^2}$  and corresponding eigenstates  $|\pm k_g\rangle = |\pm k_g\rangle_-$ . From Eq. (7) for their wave functions  $\Psi_{\pm k_g}^{(-)}(x)$  we see that the state  $|+k_g\rangle$  is mostly located on the right wire, while the state  $|-k_g\rangle$  on the left one. For  $\tilde{J} \geq 1/2$ , the two minima merge into a single global minimum, located at  $k_x^{(0)} = 0$  (see inset of Fig. 3).

Non-interacting bosons at zero temperature occupy for  $\tilde{J} < 1/2$  an equally weighted superposition of the two lowest-energy states  $|\pm k_g\rangle$  [we assume the same number of particles in each wire, see Eq. (7)]. Hence, the ground state for total particle number  $M$  is given by  $|G\rangle = 2^{-M/2} (|k_g\rangle + e^{i\theta} |-k_g\rangle)^{\otimes M}$  with an arbitrary phase  $\theta$ . The difference  $2k_g$  of the momentum components of this state introduces a length scale in the  $x$ -direction, leading to a periodic spatial modulation of the particle density

$$\rho(x) = \langle \Psi_L^\dagger(x) \Psi_L(x) \rangle = \langle \Psi_R^\dagger(x) \Psi_R(x) \rangle \sim \cos(2k_g x - \theta) + \text{const}, \quad (8)$$

and of the chiral current

$$j_C(x) = j_L(x) - j_R(x) \sim \tilde{J} \cos(2k_g x - \theta) + 2\tilde{J}^2,$$

where  $j_{L(R)}$  denotes the probability current in left (right) wire. This represents the vortex phase. On the contrary, for  $\tilde{J} \geq 1/2$ , we find a Meissner phase with constant particle densities in both wires, and the constant chiral current  $j_C$  reaching its maximum.

Non-interacting fermions at zero temperature occupy all states with energies below the chemical potential  $\mu$ , and their density  $\rho$  is always constant such that no vortex phase is present. However, the chiral current, depending on the chemical potential  $\mu$ , allows to distinguish the fermionic analog of the two bosonic phases. In Fig. 3, the chiral current is shown as a function of  $\mu$ , normalized

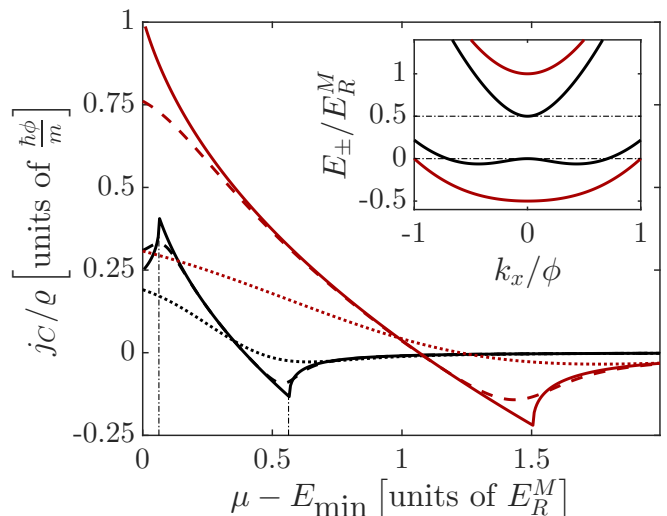


FIG. 3. (Color online) Chiral current  $j_C$  for non-interacting fermions normalized by the particle density  $\rho$  as a function of the chemical potential  $\mu$  of the lowest band for different values of the rescaled coupling  $\tilde{J}$ , black:  $\tilde{J} = 0.25$ , red:  $\tilde{J} = 0.75$  and for different ratios of temperature and coupling  $k_B T/J = 0$  (solid),  $k_B T/J = 0.1$  (dashed) and  $k_B T/J = 0.5$  (dotted).  $E_{\min}$  denotes the respective minimum energy of the lowest band. Inset: Corresponding band structure. The upper band for the coupling  $\tilde{J} = 0.75$  (red) has much higher energy (not visible in the inset).

by the particle density  $\rho$  (solid lines for zero temperature). We observe a non-analytic behavior of the current at values of  $\mu$  where the Fermi surface changes its topology, i.e. the system undergoes a Lifshitz transition [44]. For  $\tilde{J} < 1/2$ , which for particles with bosonic statistics would correspond to a vortex phase, two such Lifshitz transitions occur. The first one, which is only present for  $\tilde{J} < 1/2$ , takes place when the chemical potential touches the maximum of the lower band. The second one, existing for any non-vanishing coupling  $\tilde{J}$ , occurs when the chemical potential touches the bottom of the upper band. Hence, the presence and absence of the first Lifshitz transition determined by the form of the lowest band represents the fermionic analog to the bosonic vortex and Meissner phase, respectively.

At finite temperatures the non-analyticities in the chiral current are smeared out, but still visible for temperatures much smaller than the band gap (see dashed lines in Fig. 3). To resolve the non-analyticities in the chiral current in an experiment, the temperature has to be sufficiently low compared to energy scales set by coupling  $J$  and flux  $\phi$ . For the double wire with subwavelength separation discussed in Sec. III B 1, these non-analyticities should be observable with current experimental technology (dashed lines in Fig. 3). On the contrary, for smaller couplings strengths, typical for standard setups with wire separation  $\lambda/2$ , the chiral current is featureless. For details on the achievable coupling parameters, we refer to Sections III A and III B 2 [45].

Finally, we note that the phase distinction for both, the fermionic and the bosonic case, is determined by low momentum properties of the bands. Hence, it can be found likewise in the continuous double wire and in the discrete two-leg ladder.

#### D. Fractional quantum Hall states in coupled atomic wires

The FQH effect is the paradigmatic example of strongly correlated phases of matter that can emerge in topological bands. It typically occurs when a band with a non-zero Chern number is partially filled by strongly interacting particles. For certain rational filling factors of the band, interactions lead to incompressible states that can host anyonic fractionally charged excitations. The typical hierarchy of energy scales where this occurs is characterized by an interaction strength that is much larger than the band width but much smaller than the band gap, hence the interest in flat bands. While this phenomenon can occur both for fermionic and bosonic particles, the filling factor at which FQH states appear depends on the statistics of the particles. For example, the most prominent FQH state for fermions appears at filling  $1/3$  whereas its bosonic counterpart emerges at filling  $1/2$ . While the FQH effect was experimentally discovered in partially filled Landau levels of a 2D electron gas exposed to a strong perpendicular magnetic field, i.e., for electrons, many theoretical studies showed its realization in the context of cold atomic gases, both for bosons and fermions, in various setups such as rotating traps [46–48], optical lattices with an artificial gauge field [49, 50], optical flux lattices [9, 51], and in Chern insulators [52–54] (for reviews see [55–57]).

Below, we investigate the realization of bosonic FQH states such as Laughlin states [25] in an array of coupled wires where the non-interacting part of the Hamiltonian is given by Eq. (1). The natural interaction between the bosonic atoms, microscopically stemming from  $s$ -wave scattering, is an on-site interaction in the discrete  $y$ -direction and a contact-interaction in the  $x$  direction. In first quantization,  $H_I$  is hence given by

$$H_I = U \sum_{i < j} \delta(x_i - x_j) \delta_{y_i, y_j}. \quad (9)$$

Physically, this model is in between the HH model for bosons with on-site interactions and a model of bosons with contact interactions in a rotating trap, which both were shown to host the  $\nu = 1/2$  Laughlin state in Ref. [49, 50] and Ref. [46], respectively. Intuitively, we hence also expect this to be the case in the present model.

Interestingly, the present model is also from a formal analytical perspective in between the lowest Landau level (LLL) in the continuum and the HH on a lattice. Relating the lattice to the continuum problem, a modified HH model with longer ranged hopping known as the Kapit-Mueller model has been constructed in Ref. [58].

It features an exactly flat lowest band spanned by the same single-particle states as the lowest Landau level, simply restricted to the discrete positions of the lattice sites. Then, as the bosonic  $1/2$  Laughlin state is the exact ground state of the half filled LLL annihilating the contact interactions, its restriction to the discrete lattice is the exact ground state of the bosonic Kapit-Mueller model with on-site interactions [58]. For the present semi-continuous HH model, the lowest band is exactly flat in the limit  $J \rightarrow \infty$ , i.e. without introducing longer range hoppings, and the single particle states that span it are those of the LLL, restricted to the semi-continuous geometry of the coupled wires. As  $H_I$  in Eq. (9) is simply the contact interaction from the continuum restricted to the coupled wires, the concomitant restriction of the  $1/2$  Laughlin state from the LLL annihilates these interactions and thus must become the ground state of our present model for large  $J$ .

For finite systems and with the experimentally realistic parameters  $J = 0.05E_R, l_B = 4\lambda$ , the occurrence of a Laughlin state is hard to assess analytically. In the remainder of this section, using exact diagonalization, we hence numerically investigate this situation, focusing on the emergence of the  $\nu = 1/2$  Laughlin state in a system with periodic boundary conditions. We provide strong evidence for the occurrence of this state using both energy and entanglement spectroscopy, and give a physical picture for the resulting phase diagram of the model as a function of  $J$ . As an additional probe for the robustness of the Laughlin phase, we carefully checked that the groundstate manifold is stable under flux insertion in both directions.

##### 1. Energy spectroscopy

As commonly done in the study of FQH systems both in the continuum and on a lattice [54], we use the so called flat band approximation: we project the interacting Hamiltonian to the lowest band of the single-particle model, neglecting the admixture of all other bands as well as the band dispersion. This is a valid approximation as long as the interaction strength is much larger compared to the band width and much smaller than the band gap. We consider  $N_B$  bosons in a system of  $N_y$  coupled wires of length  $N_x l_B$ , so that the system is pierced by  $N_x N_y$  magnetic flux quanta and the filling of the lowest band is given by  $\nu = \frac{N_B}{N_x N_y}$ . This allows us to diagonalize simultaneously the Hamiltonian and the total momentum operator in both directions, defining thus two quantum numbers  $(K_x, K_y)$  for every state.

We focus on the  $\nu = 1/2$  filling where the bosonic Laughlin state is a natural candidate for describing the ground state. On the torus, it exhibits a characteristic two-fold degeneracy due to many-body magnetic translation invariance [59]. However, this degeneracy is lifted in finite lattice systems, such as the one considered here and the energy splitting  $\delta$  between the two lowest energy

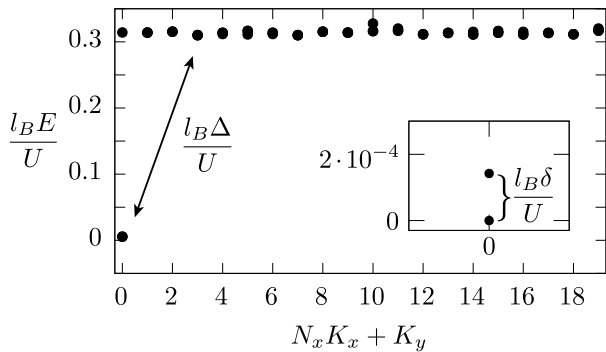


FIG. 4. Spectrum of the interaction Hamiltonian (9) for  $N_B = 10$ ,  $N_x = 2$ ,  $N_y = 10$ ,  $l_B = 4\lambda$  and  $J = 0.05E_R$ . The energy levels are plotted with respect to a linearized momentum:  $N_x K_x + K_y$ . The inset shows a zoom on the ground state manifold which is quasi two-fold degenerate as expected for the  $\nu = 1/2$  Laughlin state. The energy splitting  $\delta$  between the ground states and the energy gap  $\Delta$  are defined graphically in the figure.

states should be much smaller than the energy gap  $\Delta$  to the third lowest energy state. A typical energy spectrum for the parameters identified in Section III is shown in Fig. 4 for  $N_B = 10$ ,  $N_x = 2$  and  $N_y = 10$ . It shows the expected quasi two-fold degenerate ground state manifold (with an energy splitting  $\delta = 1.4 \cdot 10^{-4} U/l_B$ ) separated by a gap  $\Delta = 0.3 U/l_B$  from higher energy states. Depending on the geometry investigated, the ground states appear in different momentum sectors. These momentum sectors can be predicted [54] and we checked that our numerical results match these predictions.

To investigate more generically the role of interaction in our model, we restrict ourselves to the case  $\phi = 2\pi/a$  in Eq. (3). This can be done without loss of generality since a generic  $\phi$  can be mapped onto the  $\phi = 2\pi/a$  case via a rescaling of the length in the  $x$  direction and a change of the recoil energy. For this case, we show the energy gap as a function of the hopping between the wires for  $N_B = 10$  and different aspect ratios in Fig. 5. The aspect ratio seems to have an important effect on the stability of the Laughlin phase. Indeed, while for  $(N_x = 2, N_y = 10)$  the gap is much more stable with increasingly large  $J$ , the gap decreases clearly for  $(N_x = 4, N_y = 5)$  and even more for  $(N_x = 5, N_y = 4)$ . As we explain below, the crucial figure in this context is actually not the aspect ratio, but only  $N_y$ . The ostensible dependence on the aspect ratio is simply due to the fact that, for computational reasons, we cannot increase  $N_y$  without decreasing  $N_x$  at the same time.

The  $N_y$  dependence in the stability of the FQH phase can be physically understood at an intuitive level when looking at Eq. (3). With increasing  $J$ , the localization length of the lowest Wannier function in  $x$ -direction (at a given  $k_y$ ) decreases as  $J^{-(1/4)}$ . The number  $N_y$  then determines how many such equidistantly spaced orbitals there are per magnetic length  $l_B$  in  $x$ -direction.

At small enough  $N_y$ , these Wannier orbitals have virtually no overlap in  $x$ -direction, and hence allow the bosons to avoid the contact interaction, even in trivial product states forming a charge density wave (CDW). We hence expect in agreement with Fig. 5 that in finite systems with a given  $N_y$ , the Laughlin phase breaks down with increasing  $J$ , at a critical  $J_c$  that increases with  $N_y$ . This picture will be corroborated by the subsequent entanglement spectroscopy. Note that these findings are by no means in contrast to the above analytical arguments stating that for  $J \rightarrow \infty$  the ground state in the thermodynamic limit will be the exact Laughlin wave-function, but rather reflect a simple order of limits problem. This is because for  $N_y$  going to infinity, the discrete  $k_y$  values will become dense, and thus there will be an overlap of neighboring Wannier functions for arbitrary  $J$ .

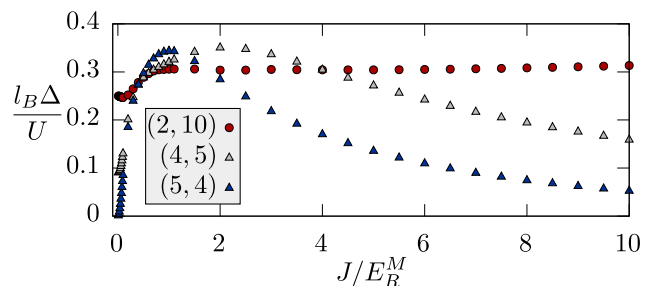


FIG. 5. (Color online) Energy gap between the second and the third lowest energy states for  $N_B = 10$ ,  $\phi = 2\pi/a$  and different aspect ratios as a function of the inter-wire hopping. The different system sizes are indicated by the values of  $(N_x, N_y)$  in the legend.

## 2. Entanglement spectroscopy

The two-fold degeneracy of the ground state is only a necessary condition for the system to be in the Laughlin phase. Indeed, a charge density wave (CDW), breaking translational symmetry, would also exhibit the same ground state degeneracy and is a known competing phase. Unlike symmetry breaking phases, topological phases do not possess a local order parameter that could be computed to probe the nature of the phase and are, thus, difficult to identify unambiguously, especially in numerical studies. To solve this issue, building upon the concept of entanglement entropy, Haldane and Li introduced the orbital entanglement spectrum (OES) [60], i.e. the spectrum of the reduced density matrix of a subsystem defined by a subset of the single particle orbitals. It allows to identify the edge theory of the ground state and, in many cases, the corresponding topological phase. For torus geometries and lattice systems, the particle entanglement spectrum (PES), a concept closely related to the OES, is a very practical tool to identify FQH states [61]. It is defined through a partition of the system in two subgroups  $A$  and  $B$ , made of  $N_A$  and  $N_B - N_A$  particles.

The PES is the spectrum of  $H_A = -\log \rho_A$  where  $\rho_A$  is the reduced density matrix obtained by tracing out the  $B$  particles and  $H_A$  is called the entanglement Hamiltonian. As  $\rho_A$  commutes with the total momentum operators for particles in the  $A$  part, we use these operators quantum numbers ( $K_{x,A}, K_{y,A}$ ) to block-diagonalize  $\rho_A$ . Unlike the OES in which the geometry of the system is altered, the geometry is unchanged by this procedure and the PES allows to access the physics of the bulk excitations.

For *ideal FQH model states*, such as the Laughlin wavefunction, the PES is made of a number of levels equal to the number of quasihole-states corresponding to the system size under investigation. For example, if we consider the  $\nu = 1/2$  Laughlin state on the torus with 4 particles and trace over two of them, the PES will reflect the Laughlin quasihole states with two particles and four quasipoles: not only the number of levels in the PES is then equal to 20, i.e. the number of quasihole-states, but the eigenstates of  $H_A$  are precisely quasihole-states as they are zero energy states of the contact interaction. All other eigenstates of the reduced density matrix have zero eigenvalues and are thus associated with levels at infinite entanglement energy in  $H_A$ . For any given number of particles and quasipoles, the number of quasihole states can be predicted using Haldane's generalized exclusion principle [62] and are thus direct fingerprints of the anyonic nature of the excitations. For the  $\nu = 1/2$  Laughlin state on the torus, the number of such states with  $N$  particles in  $N_\phi$  flux quanta is given by  $\mathcal{N}(N, N_\phi) = N_\phi \frac{(N+n-1)!}{N!n!}$ , where  $n = N_\phi - 2N$  is the number of quasipoles [63]. In the PES framework,  $N$  should be replaced by  $N_A$  and  $N_\phi$  by  $2N$  in the previous formula.

*Away from ideal model states* but still in the same FQH phase, the PES generically does not exhibit levels at infinite energy, but still displays a significant gap below which the number of states is still given by the number of quasihole-states. When this is the case, we conclude that the state is in the same topological phase as the model state. Unlike the counting of quasihole-states in the energy spectrum, the entanglement spectrum was shown to be able to distinguish between a CDW and a FQH state [64]. Indeed, in the case of a CDW ground state at filling  $1/2$ , the total number of states in the PES is given by  $2\binom{N}{N_A}$ , which in the previous example gives only 12 states.

The entanglement spectrum for the quasi two-fold degenerate ground states of Fig. 4 for  $N_A = 5$  is shown in Fig. 6. It exhibits a clear entanglement gap below which there are 4004 entanglement levels, which is precisely the expected counting for the  $\nu = 1/2$  Laughlin state with 5 particles and 10 quasipoles. This is a strong evidence for the realization of the Laughlin phase in our model at these parameters. As we did for the energy gap, we can assess the robustness of the FQH phases by looking how the entanglement gap, both the one corresponding to the Laughlin state and the one of the CDW state, changes as the aspect ratio and the hopping strength

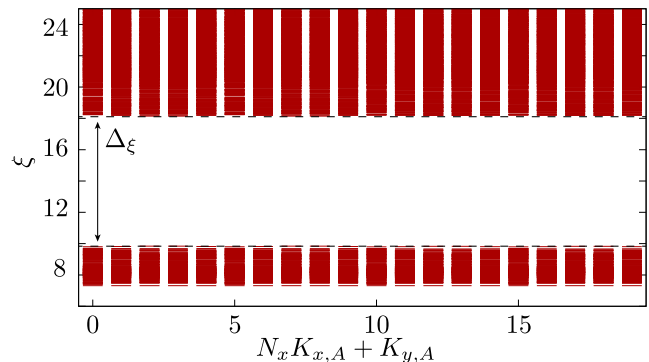


FIG. 6. (Color online) Particle entanglement spectrum for  $N_B = 10$ ,  $N_x = 2$ ,  $N_y = 10$ ,  $J = 0.05E_R$ ,  $l_B = 4\lambda$  and  $N_A = 5$  as a function of the linearized momentum of a particle in part  $A$ . The PES shows an entanglement gap  $\Delta_\xi$  indicated by the vertical arrow. The number of states below this line is equal to 4004 which is equal to the total number of quasihole states with 5 bosons and 20 flux quanta for the  $\nu = 1/2$  Laughlin state.  $\Delta_\xi$  marks the entanglement gap as discussed in the main text.

is changed. This is shown in Fig. 7 for  $N_B = 10$  and  $N_A = 4$ . In agreement with Fig. 4 and our aforementioned arguments, for  $(N_x = 2, N_y = 10)$ , the Laughlin gap dominates up to comparably large values of  $J$ , while for  $(N_x = 4, N_y = 5)$  and  $(N_x = 5, N_y = 4)$ , in decreasing order of  $N_y$ , it breaks down at smaller and smaller  $J$ . We note that the maximum entanglement gap of the Laughlin state occurs at increasing  $J$  and assumes a larger value as  $N_y$  grows. This is in line with our analytical argument that the ground state should converge towards the ideal Laughlin state with infinite entanglement gap for  $N_x, N_y, J \rightarrow \infty$ .

### III. IMPLEMENTATION WITH ULTRACOLD ATOMIC GASES

In this Section we discuss the implementation of the semi-continuous Harper-Hofstadter model described by Eqs. (1) and (2) with ultracold atomic gases in optical lattices (OL) [1, 2]. We start in Sec. III A with a discussion of the planar geometry, where the discrete direction is realized as an ordinary  $a = \lambda/2$  lattice with  $\lambda$  the optical wavelength of the laser, and coupled by laser assisted tunneling as a Raman process, which allows us to write the position dependent hopping  $J_x = J e^{i\phi x}$  with laser phases. In Sec. III B, we show how the relevant energy scales, in particular  $J$ , can be significantly increased for a double-wire (DW) with subwavelength separation. The construction of more complex, non-planar trapping geometries like arrays of rings forming cylinders or tori is discussed in Sec. III C. We show explicitly the implementation of the laser assisted tunneling in such geometries, providing the possibility to induce a large, tunable magnetic flux.

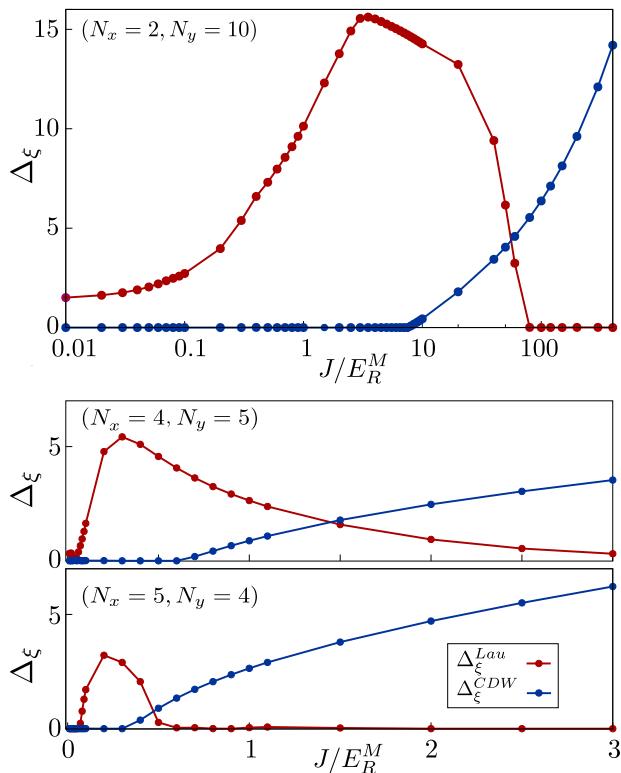


FIG. 7. (Color online) Entanglement gap, corresponding to the Laughlin state and CDW state counting, for  $\phi = 2\pi/a$ ,  $N_B = 10$ ,  $N_A = 4$  and  $(N_x = 2, N_y = 10)$  (top panel),  $(N_x = 4, N_y = 5)$  (middle panel) and  $(N_x = 5, N_y = 4)$  (bottom panel) as a function of the inter-wire hopping. Note the logarithmic scale for the horizontal axis in the top panel. In all cases, the Laughlin state emerges for intermediate values of  $J$  while at large  $J$  a CDW state is found. The  $J$  value where this transition occurs, depends strongly on the system size, more precisely on  $N_y$ , as explained in the main text.

### A. Planar geometry with optical $\lambda/2$ -lattice

A planar array of parallel wires is readily constructed with OL potentials (for the implementation of an array of parallel planes see, for example [66]). Such optical potentials for atomic motion arise as AC Stark shifts in an off-resonant laser beam in a standing wave configuration. In particular, wires with distance  $\lambda/2$  are formed by an OL potential of the form  $V_L(y, z) = V_y \sin^2(ky) + V_z \sin^2(kz)$  ( $k = 2\pi/\lambda$ ). We assume the motion in  $z$ -direction to be frozen to the lowest mode by very tight trapping. Hence, the atoms move freely in the  $x$ -direction and tunnel with an amplitude  $J_{\text{bare}} > 0$  between the wires in the transverse  $y$ -direction [see Fig. 1(a)]. We note that the assumption of a tight binding model implies  $J_{\text{bare}} \ll E_c(a) = \hbar^2/2ma^2$  for a lattice spacing  $a$ . For an ordinary OL, this energy scale is the *recoil energy*  $E_R = E_c(\lambda/2)$  associated with the wavelength of the laser [65].

A complex interwire hopping  $J_x = J \exp(i\phi x)$  with

a position-dependent phase is induced with the help of Raman-assisted tunneling [4, 13, 14, 67]: First, the natural tunneling is rendered off-resonant by means of an energy off-set  $\Delta$  between adjacent wires, i.e. a tilting of the lattice, created for example by an external magnetic field gradient. Second, resonant tunneling is restored employing a far-detuned two-photon Raman process (see Appendix C). As a result, we find the complex Raman assisted hopping  $J_x$  will be constrained by  $|J_x| = J < J_{\text{bare}}$  (see also Refs. [13, 67, 68]). Its phase  $\phi$  is determined by the momentum transfer in  $x$ -direction during the two-photon Raman process and can be adjusted by variation of the incidence angle of the two Raman lasers with respect to each other (see Sec. IIIB2 and Appendix C for a more detailed description of the laser configurations). In this Raman scheme the magnetic length  $l_B = 2\pi/\phi \gtrsim \tilde{\lambda}/2$  is bounded from below by the wavelength  $\tilde{\lambda}$  of the Raman lasers [69].

As discussed in Sec. II, to create quasi-flat Chern bands we require an inter-wire tunneling amplitude  $J$  on the order of the *magnetic (recoil) energy*  $E_R^M = \hbar^2 \phi^2 / 2m$ , i.e.  $J/E_R^M = \mathcal{O}(1)$ . In practice, this ratio should be tunable in a range from  $J/E_R^M \lesssim 0.5$  to  $J/E_R^M \gtrsim 2$ . It is not desirable to increase this ratio by simply decreasing  $E_R^M$ , as this would increase the magnetic length  $l_B = 2\pi/\phi$  and thus reduce the particle density at a given filling along with the relevant many-body interaction energies. Hence, the larger  $J$  the better, which is, however, bounded from above by  $J_{\text{bare}} \ll E_R$ . In summary, using ordinary OLs, we are constrained by the set of inequalities

$$E_R^M \sim J < J_{\text{bare}} \ll E_c(a = \lambda/2) = E_R, \quad (10)$$

and as a realistic compromise, a possible choice of parameters is  $J = 0.05E_R, l_B = 4\lambda$ . Then, the ratio  $J/E_R^M = 0.8$  and the flatness ratio of the lowest band is 137.

From an experimental viewpoint, larger energy scales  $E_R^M \sim J \sim E_R \gg k_B T$  can be crucial due to finite temperature  $T$  (see also Sec. IIC). It is thus desirable to design schemes with subwavelength interwire spacing. We will discuss this in the following Subsection for the case of a DW.

### B. Enhanced energy scales in a subwavelength double wire

In the following, we demonstrate the enhancement of the Raman assisted interwire hopping (see also Sec. IIIB2) in a DW setup with wire separation  $a = \ell \ll \lambda/2$  far below the laser wavelength, where

$$a = \ell \ll \lambda/2 \Leftrightarrow E_c(a = \ell) \gg E_R. \quad (11)$$

The construction (Sec. IIIB1) is based on the nanoscale ‘dark state’ optical potentials introduced in Ref. [35] (see also Ref. [36]). We will show that Raman assisted hopping amplitudes for typical parameters can

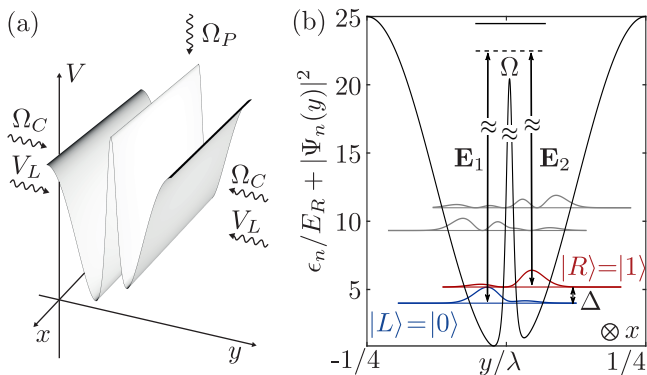


FIG. 8. (Color online) Two parallel wires with subwavelength separation  $\ell \ll \lambda/2$  are created by inserting a nanoscale optical potential barrier into a potential well  $V_L(y)$  generated by a familiar off-resonant OL. Panel (a) sketches the potential landscape with a pair of laser counterpropagating beams creating  $V_L$ . Two further lasers with Rabi frequencies  $\Omega_P$  and  $\Omega_C$  create the nanoscale barrier. Panel (b) shows the potential and wavefunctions at fixed position in  $x$ -direction. Note the small displacement  $y_0 \sim 0.1a_H$  of the barrier, w.l.o.g. towards positive  $y$ , that leads to the formation of distinct left- and right states (resp. ground  $|0\rangle = |L\rangle$  and first excited state  $|1\rangle = |R\rangle$ ) separated by an energy offset  $\Delta$ . Via far detuned Raman transitions with frequency detuning  $\delta\omega \approx \Delta/\hbar$ , resonant tunneling is restored and a spatially varying phase is induced due to a finite momentum transfer  $\delta k_x = k_{1,x} - k_{2,x}$  in  $x$ -direction.

reach values  $J \sim E_R$  (Sec. III B 2), more than one order of magnitude larger than those obtained in standard OL setups [13, 14]. Furthermore, this represents by no means a fundamental upper limit for setups featuring subwavelength structures. In parallel to this enhancement of the Raman assisted interwire hopping, the magnetic flux has to be increased to satisfy the requirement  $J/E_R^M = \mathcal{O}(1)$ . In our concrete example, a magnetic length  $l_B \sim \lambda$  is sufficient to obtain  $E_R^M \sim J \sim E_R$  (see below). This can be achieved by ordinary Raman assisted tunneling techniques (see Sec. III B 2).

### 1. Subwavelength double wire

A DW separated by a subwavelength distance is obtained using the nanoscale ‘dark state’ optical potentials introduced recently in Ref. [35] (see also Ref. [36]). Inserting such a barrier into a potential well, created, for example, as a 1D optical wire in a standard OL setup, we can split this wire into two subwires (see Fig. 8(a)). These subwires feature a spatial separation far below the laser wavelength, comparable to the typical size of the groundstate wave function of the potential well of the original OL (see Fig. 8(b)).

To produce a DW configuration extending in the  $x$ -direction, we consider, in the  $y$ -direction, a single potential well of a standard 1D off-resonant OL  $V_L(y) =$

$V_y \sin^2(ky)$  with height  $V_y$  (see Fig. 8). In the harmonic approximation, this potential well is characterized by the trapping frequency  $\hbar\omega_T \approx \sqrt{4V_y E_R}$  and by the size of the ground state wave function  $a_H = \sqrt{\hbar/(2m\omega_T)}$ . Following reference [35], the nanoscale barrier is added as a nonadiabatic optical potential

$$V_{na}(y) = E_R \frac{\epsilon^2 \cos^2(k(y - y_0))}{[\epsilon^2 + \sin^2(k(y - y_0))]^2} \quad (12)$$

for the dark state in an atomic  $\Lambda$ -system created using two additionally applied lasers, a moving wave with Rabi frequency  $\Omega_P$  constant in the  $x$ - $y$ -plane and a standing wave  $\Omega_C(y) = \Omega_C \sin(k(y - y_0))$  (see the Appendix C for details on the atomic level scheme). Hereby,  $\epsilon = \Omega_P/\Omega_C \ll 1$  is an external parameter, controlled by the lasers. It determines the subwavelength width ( $\ell \sim \epsilon/k \ll \lambda/2$ ) and the height ( $\sim E_R/\epsilon^2$ ) of the barrier which appears around  $y_0$ . Physically, this potential barrier is caused by the rapid change of the identity of the dark state in the subwavelength region of width  $\ell$ , see the Appendix C and Ref. [35] for details. Ignoring the frozen motion in the  $z$ -direction for which we assume tight confinement, the dark state Hamiltonian takes the form

$$H_D(x, y) = - \left( \frac{\hbar^2 \partial_x^2}{2m} + \frac{\hbar^2 \partial_y^2}{2m} \right) + V_L(y) + V_{na}(y). \quad (13)$$

For  $\epsilon \ll 1$ , the eigenstates of  $H_D$  are grouped into pairs of states with small energy offset  $\Delta \ll \hbar\omega_T$ . Different pairs are separated by a large gap  $E_{\text{gap}} \approx 2\hbar\omega_T$ . In the following, we can hence restrict to the lowest pair formed by ground  $|0\rangle$  and first excited state  $|1\rangle$ . Due to a small displacement  $y_0 \ll a_H$  of the barrier with respect to the center of the harmonic trap, one of these two states (as in every pair) is mostly localized on the left, one on the right of the barrier, with only a small fraction leaking through. We hence identify a DW system consisting of distinct left  $|L\rangle \equiv |0\rangle$  and right  $|R\rangle \equiv |1\rangle$  wire, respectively (for the configuration shown in Fig. 8 with the barrier displaced to the right, i.e.  $y_0 > 0$ ). We are interested in a situation where the wires are well separated. This means that the localization parameter  $\text{Loc} \equiv 1/2(P_L + P_R)$  with  $P_L \equiv \int_{-\infty}^{y_0} dy |\langle y|L\rangle|^2$ ,  $P_R \equiv \int_{y_0}^{\infty} dy |\langle y|R\rangle|^2$  has to be close to unity. In the following, we hence keep  $\text{Loc} > 0.9$ , balancing between the spatial separation of the wires and the strength of the interwire coupling (see below) related to the spatial overlap of their wave functions.

Summarizing, we have created a double wire with interwire distance  $\ell \ll \lambda/2$  far below the laser wavelength. This provides the opportunity to obtain Raman-assisted interwire couplings much larger than in a familiar optical lattice, because the *a priori* bare hopping amplitudes can be much larger than for a standard OL, as shown in the following subsection.

## 2. Enhanced Raman-assisted tunneling amplitude

We now discuss a Raman-assisted tunneling scheme for the subwavelength DW, where complex tunneling phases can be obtained in a Raman assisted tunneling scheme as described above. Our goal is to maximize the Raman assisted tunneling amplitude  $J$  and to achieve simultaneously a large magnetic flux  $E_R^M/J = \mathcal{O}(1)$ . We compare to previous results obtained in ordinary OLs [13, 14].

The tunnel coupling between the wires is generated by two additional Raman beams  $\mathbf{E}_1$ ,  $\mathbf{E}_2$  with frequencies  $\omega_1$ ,  $\omega_2$  and wave vectors  $\mathbf{k}_1$ ,  $\mathbf{k}_2$  located in the  $x$ - $y$ -plane. They drive a far-detuned two-photon transition via an auxiliary level (Figure 8, detailed in Appendix C). Adiabatic elimination of the auxiliary level leads to an additional time-dependent driving term

$$H_{RM}(x, y, t) = \Omega \cos(\delta k_x x + \delta k_y y - \delta \omega t), \quad (14)$$

in the full Hamiltonian  $H(t) = H_D + H_{RM}(t)$ , where  $\Omega$  is the effective two-photon Rabi frequency,  $\delta \omega = \omega_1 - \omega_2$  the frequency detuning and  $\delta \mathbf{k} = \mathbf{k}_1 - \mathbf{k}_2$  the momentum transfer. Choosing  $\delta \omega \approx \Delta/\hbar$ ,  $H_{RM}$  induces resonant tunneling between the two wires whose amplitude is in the perturbative regime  $\Omega \ll \hbar \delta \omega$  given by

$$J_x \approx \frac{\Omega}{2} \langle L | e^{-i\delta k_y \hat{y}} | R \rangle e^{-i\delta k_x x} \equiv J e^{i\phi x}. \quad (15)$$

Importantly, the matrix element  $|\langle L | e^{-i\delta k_y \hat{y}} | R \rangle| = \mathcal{O}(1)$  is increased in our setup by at least one order of magnitude compared standard OLs where we have  $|\langle L | \exp(-i\delta k_y \hat{y}) | R \rangle| \sim J_{\text{bare}}^{\text{OL}}/E_R \lesssim \mathcal{O}(1/10)$  between any two adjacent wires  $L$  and  $R$  [13]. This is caused by the larger spatial overlap of the wave functions and leads to the strongly enhanced tunneling amplitudes in the subwavelength DW.

Our goal is now to find the maximum possible Raman assisted tunneling amplitude (c.f. Fig. 9). Here, we investigate the overall behavior of the tunneling amplitude as a function of the driving strength  $\Omega$ . This requires to access the non-perturbative strong driving regime using a numerical Floquet analysis. As shown in the inset of Fig. 9, the tunneling amplitude follows the common trend [13, 67, 68]: A linear growth with the driving in the perturbative regime before the onset of higher order effects diminishing the coupling for strong driving  $\Omega \gtrsim \hbar \delta \omega$ . It is renormalized due to time-dependent AC-Stark shifts of the individual levels  $|L\rangle$  and  $|R\rangle$ . For details on this higher order effects, a systematic perturbation theory in powers of  $\Omega/\hbar \delta \omega$  and the numerical procedure, we refer to Appendix D.

Due to the large tunneling matrix element in Eq. (15), the maximum amplitude of the tunnel coupling between the wires is strongly enhanced compared to the results of Ref. [13] for the standard setup with a tilted OL. As an example, for the tilted OL with the amplitude  $V_0 = 9E_R$ , the amplitude of the Raman assisted tunneling between the nearest sites is bounded by the bare

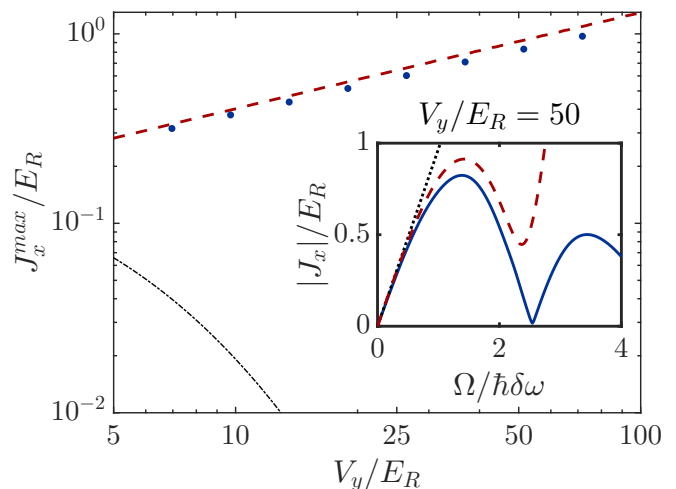


FIG. 9. (Color online) Maximal achievable Raman induced tunneling rate between two atomic nanowires with subwavelength separation as a function of the strength of the external trapping potential  $V_y$  (Blue dots: numerical Floquet analysis, Red dashed line: second order perturbation theory in an expansion of an effective Hamiltonian in powers of  $\Omega/\hbar \delta \omega$ ). For comparison, the bare tunneling rate of a standard OL is shown (black dashed-dotted line), bounding the Raman assisted hopping in the corresponding tilted OL [13, 70]. Inset: tunneling rate as a function of the driving amplitude, the two-photon Rabi frequency  $\Omega$  (Numerical Floquet analysis (blue), zeroth (black dotted) and second (red dashed) order perturbation theory).  $\epsilon \approx 0.1$ ,  $y_0 \approx 0.1a_H$ ,  $\delta k_y = 2k$  and  $\delta \omega = 1.1\Delta/\hbar$  have been chosen to maximize resonant tunneling.

tunneling  $J_b = 0.02E_R$  [13]. Using the same OL with the subwavelength barrier placed in one of its wells, one can achieve an order of magnitude increase,  $J_x \approx 0.2E_R$ , of the tunneling amplitude (see Fig. 9).

In contrast to standard OLs, the Raman assisted tunneling amplitude in our setup can be further enhanced by increasing the amplitude of the trapping potentials  $V_y$ , as shown in Fig. 9. This results in the increase of the level separation  $\Delta$  leading to a larger value  $\Omega_{\text{max}} \sim \hbar \delta \omega \sim \Delta$  where the maximum tunneling amplitude  $J_x \sim \Omega_{\text{max}}$  is reached. This overcomes a decrease of the tunneling matrix element  $\langle L | e^{-i\delta k_y \hat{y}} | R \rangle$ . Quite remarkably, the tunneling amplitude  $J_x$  reaches the values of  $\sim 1E_R$  for  $V_y = 100E_R$  (c.f. Fig. 9).

At the same time, a large flux  $(\hbar^2 \phi^2/2m)/J = \mathcal{O}(1)$  is achieved using the following laser configurations: We take laser  $\mathbf{E}_1$  to be  $\sigma_+ = -(\mathbf{e}_z + i\mathbf{e}_x)/\sqrt{2}$  polarized and propagating along the  $y$ -direction. The laser  $\mathbf{E}_2$  propagates the  $x$ - $y$ -plane with an incidence angle  $\theta$  with respect to  $\mathbf{E}_1$ . The momentum transfer during the two-photon process is thus  $\delta \mathbf{k} = \mathbf{k}_1 - \mathbf{k}_2$ . By variation of  $\theta$ , we can hence adjust the phase  $\phi = \delta k_x$ , up to large fluxes  $(\hbar^2 \phi^2/2m)/E_R = \mathcal{O}(1)$  (for  $\theta \approx \pi/2$ ).

To summarize, our discussion shows that tunneling amplitudes  $J \sim E_R$  can be reached in a subwavelength DW, which are enhanced by more than one order of magnitude compared to familiar OLs. In addition, this

scheme allows one to achieve fluxes  $E_R^M \sim J$  compatible with the enhanced hopping.

### C. Non-planar trapping geometries: cylinder and torus

Below we describe the realization of optical potentials for ultracold atoms with cylindric rotational symmetry — the cylinder consisting of an array of rings (Sec. III C 1) and the torus (Sec. III C 3). The construction is based on Laguerre-Gaussian (LG) laser beams. Similar beams allow also to thread artificial magnetic field flux through the surface of each geometry and realize the scenario of the flat band Hamiltonian (1). All beams are set deep in the paraxial regime, where beam waist  $w_0$  satisfy  $w_0 \gg \lambda$ , and the constructed lattices will feature standard interwire separations of  $a = \lambda/2$ .

#### 1. Cylindric array of rings

The cylinder geometry [see Fig. 1(b)] can be naturally obtained using a laser mode with a cylindric symmetry, such as a LG beam (see Refs. [21–23, 71–73] for theory description and Refs. [74–77] for the experimental state of the art). The spatial mode of the LG beams is indexed by integers  $l$  and  $p$  (we consider here  $p = 0$ ) which we refer to as  $LG_{p,l}$ . Its electric field amplitude is

$$\mathbf{E}_0(\rho, \varphi, y) = \epsilon_0 E f_{p,l}(\rho, y) e^{il\varphi} e^{iky}, \quad (16)$$

where the  $\epsilon_0$  is the polarization vector, taken to be  $\sigma_+ = -(\mathbf{e}_z + i\mathbf{e}_x)/\sqrt{2}$ . Here  $E$  denotes the field strength. We have chosen cylindrical coordinates with azimuthal angle  $\varphi$  and  $\rho = \sqrt{x^2 + z^2}$  the distance to the symmetry axis  $\mathbf{e}_y$ . The rotationally invariant field amplitude is

$$f_{p,l}(\rho, y) = \frac{w_0}{w_y} \sqrt{\frac{2p!}{\pi(p+|l|)!}} \xi^{|l|} L_p^{(|l|)}(\xi^2) e^{-\xi^2/2}, \quad (17)$$

with  $\xi = \sqrt{2}\rho/w_y$ ,  $w_y = w_0\sqrt{1+(y/y_R)^2}$ , and  $w_0$  is the paraxial waist of the beam. Further, the Rayleigh range  $y_R = w_0^2\pi/\lambda$  and  $L_p^{(|l|)}$  is a generalized Laguerre polynomial (for  $p = 0 : L_0^{(|l|)}(\xi) = 1$ ). The plane  $y = 0$  in this description is the focal plane of the LG beam.

The LG beam creates a potential [see Fig. 10(a)]

$$V_L(\mathbf{r}) = V_m |f_{p,l}(\rho, y)|^2, \quad V_m < 0. \quad (18)$$

which in radial direction contains a Gaussian minimum located at finite position of  $r_* = w_0\sqrt{l/2}$ , thus realizing a potential well corresponding to the side surface of a cylinder, when  $y/y_R \ll 1$  [see Fig. 10(b)].

On top of the cylindrical potential we add a lattice potential  $V_L(y) = V_y \sin^2(ky)$  splitting the cylindric landscape into a series of parallel ring traps separated by  $a = \lambda/2$  distance [see Fig. 10(c),(d)]. It should be noted

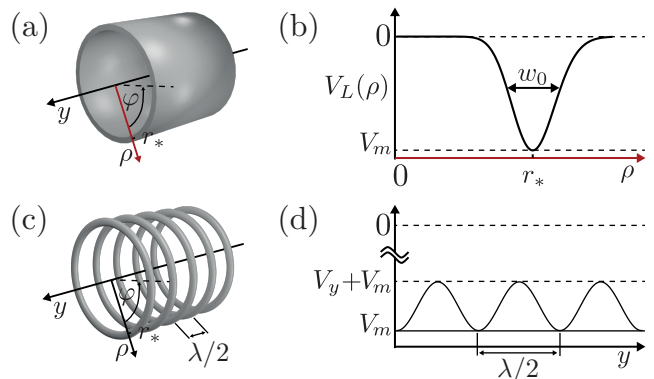


FIG. 10. (Color online). Panel (a) shows the rotationally invariant, cylindrical potential well created by a Laguerre-Gaussian beam  $LG_{0,l}$  in cylindrical coordinates. Panel (b) shows the intensity profile in the radial direction, featuring a Gaussian potential centered at finite radius  $r_* = w_0\sqrt{l/2}$  of width  $w_0$  and depth  $V_m$ . Panel (c) shows the slicing of the cylindrical potential featured in (a) by an extra standing wave potential creating a series of rotationally invariant parallel rings. Panel (d) shows the  $y$ -dependence of the resulting potential.

that the LG beams may be used in a fashion similar to Sec. III B 1 to create a subwavelength barrier with ring shape and in the end the two parallel rings with subwavelength separation  $\ell \ll \lambda$ .

#### 2. Raman-assisted tunneling

Below we discuss specific features of the Raman-induced hopping in the cylindric geometry. We start by explaining the creation of a synthetic magnetic field. Then, we discuss how to couple many rings using just two lasers, addressing residual focusing effects. They define a maximal achievable total size of the system, allowing to couple together several tens of rings for which the Hamiltonian (1) is realized.

The Raman scheme for laser-assisted hopping proceeds in analogy to the one discussed in Section III B. First, a magnetic field gradient creates a local energy offset between neighboring rings. Second, the rings are coupled via a Raman process tuned to that offset. The non-standard part is however the choice of the LG laser beams for the lasers creating the two-photon transition.

We employ two  $\sigma_+$  polarized LG beams:  $LG_{0,l_1}$  and  $LG_{0,l_2}$ , counterpropagating in the  $y$ -direction. The azimuthal complex phase carried by the LG beams [see Eq. (16)] amounts to a total angular momentum transfer during the two-photon process. In analogy to Eq. (15), this leads to a tunneling phase of  $\phi = (l_1 - l_2)/R$  where  $R$  denotes the radius of the cylinder. The fundamental limit for the complex phase  $\phi$  is the diffraction limit, which is bounded by  $\phi^{-1} > \phi_c^{-1} = \lambda_R/2$  with  $\lambda_R$  the wavelength of the Raman lasers [41]. Even far from the diffraction limit, for  $\phi/\phi_c = 1/8$ , we obtain  $\hbar^2\phi^2/2m = 1/16E_R$  and

hence  $J/(\hbar^2\phi^2/2m) = \mathcal{O}(1)$  in the desired regime (for realistic  $J = 0.05E_R$ , see Section II).

To simultaneously Raman-couple many wires resonantly using just two lasers with the desired amplitude  $J$ , one needs to assure that a global choice of detuning of the two lasers  $\delta\omega = \omega_1 - \omega_2$  [as discussed in Section III B 2] can be made. In the cylindrical geometry case, the local energies  $E_y$  of the rings are determined by the cylindrical optical potential (18), by the trap frequency  $\hbar\omega_T \approx \sqrt{4V_y E_R}$  of the lattice potential  $V_L(y)$  and by an additional external magnetic field gradient giving rise to an offset  $\Delta$  between adjacent rings. They read as

$$E_y = V_m \left[ 1 - \frac{y^2}{y_R^2} + \frac{y^4}{y_R^4} + \mathcal{O}\left(\frac{y^6}{y_R^6}\right) \right] + \Delta \frac{y}{a} + \hbar\omega_T. \quad (19)$$

Hence, the total difference between neighbouring rings is  $\Delta_y = E_{y+a} - E_y = \Delta + \delta_y$  where  $\delta_y$  depends non-linearly on  $y/y_R$ . This is in contrast to the planar case where  $\Delta_y = \Delta = \text{const.}$ , i.e.  $\delta_y = 0$ .

In the effective Hamiltonian (1) the presence of  $\delta_y \neq 0$  adds an extra local energy term  $\sum_y \tilde{\delta}_y \hat{n}_y$  where  $\tilde{\delta}_y = \sum_{y' \geq y} \delta_{y'}$ . To keep this extra term negligible, we hence require that

$$\tilde{\delta}_y \ll J. \quad (20)$$

This defines the maximal number  $\sim y_R \sqrt{J/V_m}/a$  of lattice rings to be resonantly coupled. This number is enlarged if the quadratic part  $\sim y^2/y_R^2$  in equation (19) is compensated by an additional anti-trapping potential, allowing  $\sim y_R \sqrt{J/V_m}/a$  lattice rings to be coupled simultaneously by a Raman process. Here  $y_R$  is limited by the separation between radial, transverse modes of  $\Delta E_\rho = \sqrt{8\hbar^2 V_m/mw_0^2}$  where  $w_0$  is the waist of the LG beams creating the cylinder. For realistic values of parameters one can construct 20 or more parallel rings.

### 3. Torus geometry

To realize a torus geometry of coupled rings, we create two copies of cylinders nested into each other. Only at the rings located at the edges, inner and outer cylinder are coupled (by laser-assisted tunneling), closing the geometry to a torus [see Fig. 1 and 11]. To suppress the hopping between the cylinders at other positions, the cylinders are implemented as state-dependent potentials for ultracold atom gas populating two hyperfine ground states  $g_1$  and  $g_2$  [78–80]. The potential felt by each atomic state contains just a single cylinder. Any hopping of atoms between the two cylinders involves a change of atomic configuration which prohibits the occurrence of (bare) tunneling processes. By a specially constructed laser-assisted hopping Raman scheme [13, 14], inner and outer cylinder can be coupled. Crucially, the state dependent potentials allows us to keep the spatial separation of

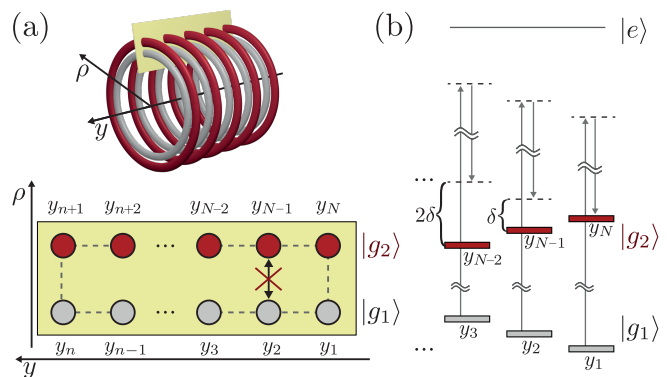


FIG. 11. (Color online). Torus geometry created by Raman-coupling ends of two coaxial cylinders. Panel (a) shows coupled rings that together create a toric geometry. Red and silver color indicate lattice sites occupied by atoms in atomic states  $g_1$  and  $g_2$  respectively. Panel (b) shows the landscape of local energies of sites in the two rings which is created by a single external magnetic field gradient. It features different tilting for the individual internal states (red as opposed to silver). This allows to resonantly Raman-couple just two rings [ $y_1$  and  $y_N$  in panel (b)].

the cylinders  $\sim \lambda$ , which is necessary for a non-negligible hopping amplitude between the two rings (see Eq. (15)).

In more detail, the laser-assisted tunneling scheme coupling only rings at the edge is constructed as follows. Since each cylinder is populated by a different atomic state, the tilts of the local energies due to external magnetic field gradient can be chosen differently [see two gradients of energies for silver and red states in Fig. 11(b)]. Two rings indexed as  $j$  and  $N - j + 1$  have the same position  $y_j = y_{N-j+1}$  in  $y$ -direction and are concentric. The difference of local energies of the outer and inner ring  $\Delta_j = E_{N-j+1} - E_j$  depends nontrivially on the position  $y_j = y_{N-j+1}$ . When engineering a Raman process, it is therefore possible to adjust the relative detuning of the Raman lasers  $\delta\omega$  to be resonant only with a single  $\Delta_j$  and off-resonant for all others [see Fig. 11(b)]. This allows to couple inner and ring only at the edges of the cylinder, i.e. at positions  $y_{j=1} = y_{j=N}$  and  $y_{j=N/2} = y_{j=N/2+1}$ , respectively. In this way, the two cylinders are closed into a torus geometry. For further details, we refer to Appendix B.

## IV. CONCLUSIONS

In this work we have proposed and studied the realization of a *semi-continuous Harper-Hofstadter model* with cold atoms in optical lattices. This model is defined in the semi-continuous position space of an array of wires. It hence naturally combines key physical aspects of recently observed lattice systems, such as the Harper-Hofstadter (HH) model [4, 14] and the two leg ladder [15], with continuum systems such as Landau levels and rotating con-

densates [46], respectively.

In the continuous lowest Landau level, both the energy dispersion and the Berry curvature are exactly flat, and the energy gap to the next higher Landau level is determined by the magnetic cyclotron frequency  $\omega_c = eB/m$ , i.e. proportional to the magnetic field  $B$ . Here instead, in Hamiltonian (3), there are two *independent* knobs for tuning (i) the magnetic length by varying the synthetic flux  $\phi = 2\pi/l_B$ , and (ii) tuning the gap along with the flatness by varying the hopping strength  $J$ . Both these knobs are readily accessible experimentally in present experiments with ultracold atomic gases, thus allowing to realize various parameter regimes.

This situation is also strikingly different from the HH on a lattice, where the flatness of the lowest (Chern) band is determined by the magnetic flux per plaquette rather than by the hopping strength, and flat bands resembling the lowest Landau level are achieved in the limit of large magnetic length. To overcome this issue, Ref. [58] proposed an extension of the HH model with flat bands at the expense of longer range hopping, and subsequently quite some effort has been devoted to identifying various mechanisms that generate approximately flat Chern bands [3, 56]. In this context, the semi-continuous HH model provides a particularly easy route towards flat Chern bands with ultracold atomic gases, where the flatness is simply tuned by the nearest neighbor hopping  $J$ .

As an illustration of how FQH states can be stabilized in the coupled wire setting, we have shown with both analytical arguments and a numerical analysis the emergence of a Laughlin phase in a system for experimentally realistic parameters. In the limit of a small  $J$  acting as a perturbative coupling between strongly correlated wires (Luttinger liquids), it is well known from renormalization group arguments how various more complex FQH states can be appear in coupled wires [28]. In the present atomic setting with flat Chern bands in the limit of large  $J$ , we identify the search for specific longer range interactions stabilizing non-Abelian FQH states in arrays of coupled wires, and their experimental realization with the cold atom toolbox as an interesting subject of future research.

We note that synthetic dimensions, where an internal degree of freedom of the atom [81] or harmonic oscillator states of a confining potential [82] are interpreted as the discrete dimension, may provide an alternative route towards experimentally realizing coupled wires. Regarding quantum Hall physics, a first study in this context [83] indicates that no FQH states are stabilized there due to the strongly anisotropic nature of the two-body interactions. A possible way around this issue is provided by the approach of using the angular variable of a photonic ring cavity [84] as a synthetic dimension, which results in spatially local interactions.

For the double-wire – the minimal setting hosting a synthetic magnetic flux – we have proposed the realization of a pair of atomic nanowires with sub-wavelength separation, which significantly increases the relevant en-

ergy scales over existing OL realizations. At effective temperatures already realized in state of the art cold atom experiments, we argue that this crucial enhancement enables the visibility of intriguing quantum phenomena in Fermi gases such as Lifshitz transitions. Generalizing these techniques to the case on more than two wires would open up entirely new possibilities for the experimental observation of strongly correlated phenomena.

The use of Laguerre-Gauss beams allows us to create non-planar coupled wire systems in cylinder- disk- and torus-geometries. A counterpart of this construction for the HH lattice model has recently been presented in Ref. [41]. We conclude by stressing another key advantage of the present semi-continuous HH model as compared to its lattice counterpart, in the context of such non-planar geometries. In the lattice version, we proposed to use tightly focused beams (see Ref. [41] and references cited there) in order to achieve lattice constants in the circumferential direction on the order of optical wavelengths. This was important to achieve energy scales – in particular band gaps – that are on the order of those found in conventional OLs. Here, as such band gaps are simply tuned by the hopping  $J$  in the discrete axial direction (see Fig. 1 (b)), where the lattice spacing is anyway (at most) the one of a conventional OL, there is no need for the additional experimental effort of tight focusing.

## ACKNOWLEDGMENTS

We thank E. Bergholtz, J. Dalibard, N. Goldman, and H. Pichler for discussions and feedback on the manuscript. Work at Innsbruck is supported by the European Research Council (ERC) Synergy Grant UQUAM, the Austrian Science Fund through SFB FOCUS (FWF Project No. F4016-N23), and EU FET Proactive Initiative SIQS. A.S. acknowledges funding by the European Research Council (ERC) grant WAS-COSYS (No. 636201).

### Appendix A: Band flatness and Berry curvature of the Hamiltonian (1)

In this appendix we provide further details on the flatness ratio and Berry curvature of the band structure, and the localization properties of the edge modes associated with the Hamiltonian (1). The characteristic energy scales are the coupling  $J$  and the magnetic recoil energy  $E_R^M = \hbar^2 \phi^2 / 2m$ .

The flatness of the bands (as described in Sec. III C 1) is described by the ratio  $F \equiv BG/BW$  of the bandwidth  $BW$  of the lowest Bloch band to the band gap  $BG$  between the lowest and the first excited band. In the limit  $J/E_R^M \gg 1$  we obtain by analogy to the standard optical

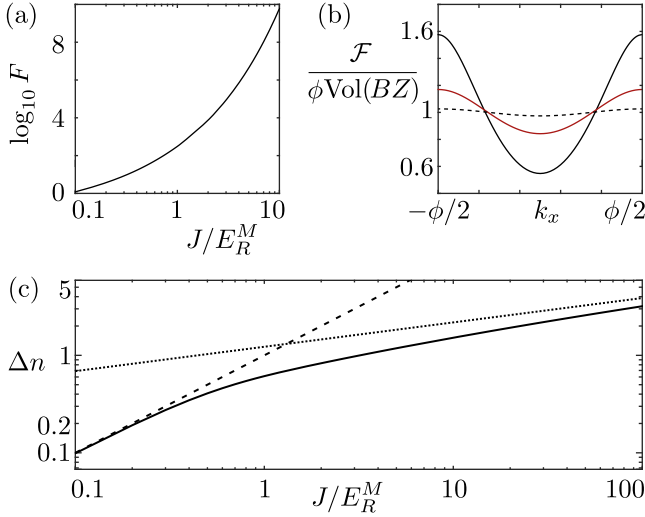


FIG. 12. (Color online) Illustration of properties of the band structure of the Hamiltonian (1). Panel (a) shows the flatness ratio  $F$  of the band as a function of  $\tilde{J} = J/E_R^M$ . Note the log scale on the  $y$ -axis. Panel (b) shows the normalized Berry curvature for different  $J/E_R^M$ . The values of the latter are 0.25 (black solid line), 0.5 (red solid line), 1.0 (black dotted line). Panel (c) shows the width of the edge mode wavefunction (for  $k_x = 0$ ) defined as  $\Delta n = \sqrt{\langle (Y - Y_{\text{edge}})^2 \rangle}/a$ . Note that  $\Delta n = 0$  indicates perfect localization of the wavefunction on the edge. The guide lines show asymptotic behavior for  $J/E_R^M \gg 1$  (dotted line) and for  $J/E_R^M \ll 1$  (dashed line).

lattice [1] approximate expressions for the band gap

$$BG \approx \sqrt{2JE_R^M} \quad (\text{A1})$$

and bandwidth

$$BW \approx 16E_R^M (J/2E_R^M)^{3/4} e^{-2\sqrt{J/2E_R^M}}/\sqrt{\pi}. \quad (\text{A2})$$

Hence, in this limit  $J/E_R^M \gg 1$ , the flatness ratio  $F$  is exponentially large. For intermediate values  $J/E_R^M = \mathcal{O}(1)$ ,  $F$  can be calculated numerically, as shown in Fig. 12(a) (note the logarithmic scale). Even for  $J/E_R^M = 1$  the flatness ratio  $F \sim 300$  is already very large. Further, together with increasing flatness of the lowest band, also its Berry curvature  $\mathcal{F}_k^\alpha = i\text{Tr} \{P_k^\alpha [(\partial_{k_x} P_k^\alpha), (\partial_{k_y} P_k^\alpha)]\}$  (see also Eq. (4)) shows increasing flatness, as indicated in Fig. 12(b).

The form of single particle wavefunctions is given by Eq. (5). The corresponding momentum sector of the Hamiltonian (3) is

$$H = \sum_{j=1}^N E_j \hat{n}_j + J \sum_{j=1}^{N-1} a_{j+1}^\dagger a_j + H.c. \quad (\text{A3})$$

where  $E_j = \hbar^2 k_j^2/2m$ ,  $k_j = k_x + \phi(j - j_0)$ . The  $E_j$  form a parabolic energy barrier. In particular, edge modes correspond to the case of  $j_0 \approx 1$  or  $j_0 \approx N$ . For large  $J/E_R^M$

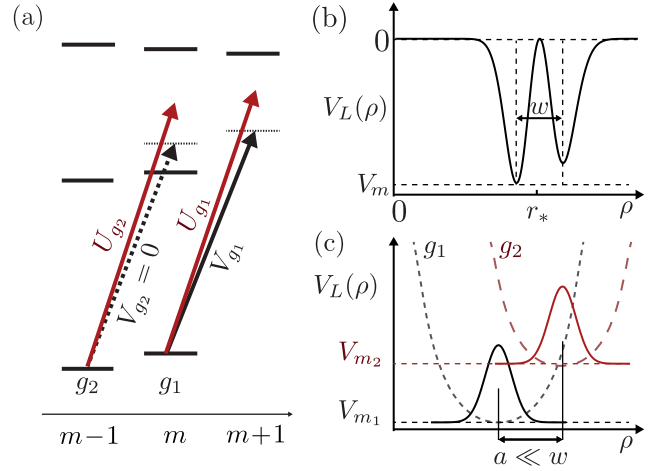


FIG. 13. (Color online) Panel (a) Atomic level scheme for the state-dependent lattice akin to Ref. [85]. Black lines indicate a  $\sigma_+$ -polarized laser tuned to a magic wavelength to make the AC-Stark shift for atoms in state  $g_2$  zero. The red laser indicate the second laser used, and symbols  $U_{g_i}, V_{g_i}$  the created optical potentials (see Appendix B for discussion). Panel (b) Constructing optical potential in the form of parallel rings using the LG mode with  $p = 1$  mode results in large ( $\sim w$ ) separation of subsequent rings in  $w \gg \lambda$  limit. Panel (c) Two rings created by a state-dependent potential. One (black, short dashes) potential well is for atoms in  $g_1$  state, other (red, long dashes) for atoms in  $g_2$  state. The resulting separation of the ground state wave functions is  $a \sim \lambda \ll w$ .

the above Hamiltonian is formally identical to the harmonic oscillator problem  $H = \frac{d^2}{dy^2} + \alpha y^2$  on the positive real axis. Mapping it to the discrete case given by (A3), for  $J/E_R^M \gg 1$  the width of the edge mode wavefunction is  $\langle (Y - Y_{\text{edge}})^2 \rangle_{GS}/a^2 \approx 3/2\sqrt{J/E_R^M}$ . Thus the width of the edge mode is

$$\Delta n = \sqrt{\langle (Y - Y_{\text{edge}})^2 \rangle}/a = \sqrt{3/2\sqrt{J/E_R^M}}. \quad (\text{A4})$$

This scaling behaviour with  $J/E_R^M$  is verified numerically in Fig. 12(c) and indicates that well localized edge modes occur when  $J/E_R^M \lesssim \mathcal{O}(1)$ .

In summary, for  $J/E_R^M \approx 1$ , the system described by Hamiltonian (1) features both (very) flat bands and well-localized edge modes. Keeping  $J$  constant and decreasing  $E_R^M$  has the effect of exponentially increasing the flatness ratio of the Bloch bands at the price of algebraic increase of the width of the edge modes given by Eq. (A4). Another effect is the decrease of the gap between the topological bands of Hamiltonian (1) as indicated by Eq. (A1), which however allows to utilize the flat band regime.

## Appendix B: Spin-dependent lattice for the torus geometry

Two coaxial, independent series of parallel rings coupled at their ends, create the torus geometry as described in Sec. III C 3. In this Appendix we detail the possible implementation with state-dependent potentials.

The radial cut through the optical potential created by the LG beams (for  $p = 0$ ), has just a single Gaussian potential well with width given by the waist  $w \gg \lambda/2$  (see Sec. III C 1). Although taking  $p = 1$  would create two ring-shaped potentials [see Fig. 13(b)], their large radial separation of order  $\sim w$  would make Raman coupling of rings of each cylinder very small.

Instead we create each ring as a state-dependent potential for atom gas in two stable states  $g_1$  and  $g_2$  which are extremal atomic states of the hyperfine manifold (similar to Ref. [85]). Such a gas is then coupled to the manifold of excited states by a  $\sigma_+$  polarized laser light in Laguerre-Gaussian mode  $LG_{l,p}$  [see Fig. 13(a) - coupling due to that laser are indicated black]. Its wavelength is chosen as a 'magic' wavelength meaning the AC-Stark shift and the created optical potential for a  $g_2$  state is zero  $V_{g_2}(\mathbf{r}) = 0$ , and nonzero for the state  $g_1$ :  $V_{g_1}(\mathbf{r})$ . Low heating rates for state-dependent potentials can be reached for atoms with large fine-structure splitting such as dysprosium and erbium [86]. A second laser beam (with a different wavelength, in 13(a) marked red) also in a LG mode creates then optical potentials for both components:  $U_{g_1}(\mathbf{r})$  and  $U_{g_2}(\mathbf{r})$ .

The potentials  $V_{g_i}$  and  $U_{g_i}(\mathbf{r})$ ,  $i = 1, 2$  can be chosen to have different radii realizing the minimum of the potential in the radial direction. This allows to microadjust the radial separation of the minima of felt by each of the components  $g_1$  and  $g_2$  on distances  $\ll w$  [see Fig. 13(c)]. As made clear in Appendices C and D this condition is sufficient and necessary to be able to reach Raman hopping amplitudes just as between two neighboring wires of the same cylinder (with a separation  $a = \lambda/2$ ).

## Appendix C: Microscopic derivation of the 'dark state' Hamiltonian

In this Appendix, we present the derivation of the dark state Hamiltonian  $H_D$  [Eq. (13)] and the time dependent potential  $H_{RM}(t)$  [Eq. (14)] resulting from a far-detuned two-photon Raman transition to an auxiliary level. For a detailed analysis of the nanoscale dark state potentials, we refer to Ref. [35] (see also Ref. [36]).

Assuming a very tight confinement in the  $z$ -direction, we consider a single atom moving in the  $x$ - $y$ -plane. Whereas it moves freely in  $x$ -direction, we introduce a harmonic confinement potential in  $y$ -direction, e.g. as a potential well of a standard 1D optical lattice with depth  $V_y$  and effective trapping frequency  $\omega_T \approx \sqrt{4V_y}E_R$  in

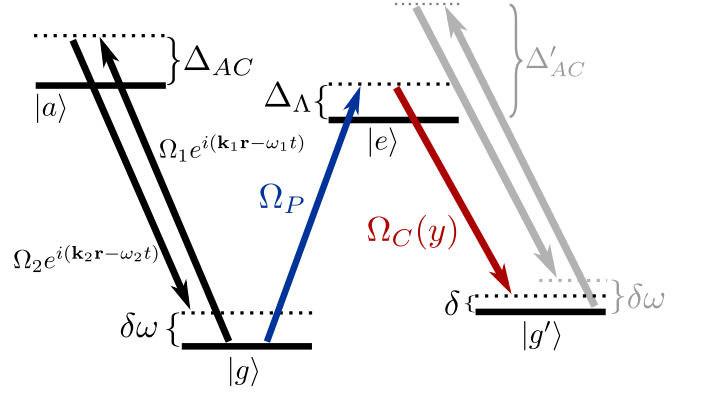


FIG. 14. (Color online) Level scheme of the atomic  $\Lambda$ -type configuration formed by the long lived ground states  $|g\rangle$  and  $|g'\rangle$  coupled via Rabi frequencies  $\Omega_P$  (blue) and  $\Omega_C(y)$  (red), respectively, to an excited level  $|e\rangle$ . Additionally, far detuned Raman beams, moving waves with amplitudes  $\Omega_1$  and  $\Omega_2$ , couple  $|g\rangle$  to an auxiliary level  $|a\rangle$  (black arrows) and  $|g'\rangle$  to  $|e\rangle$  (grey arrows).

harmonic approximation. We obtain

$$H_{\text{ext}}(x, y) = - \left( \frac{\hbar^2 \partial_x^2}{2m} + \frac{\hbar^2 \partial_y^2}{2m} \right) + \frac{1}{2} m \omega_T^2 y^2. \quad (\text{C1})$$

Internally, we consider an atomic  $\Lambda$ -type configuration where two long lived ground states  $|g\rangle$  and  $|g'\rangle$  are coupled to an excited state  $|e\rangle$  via a weak probe laser with Rabi frequency  $\Omega_P$  (constant in the  $x$ - $y$ -plane) and a strong control laser, a standing wave with Rabi frequency  $\Omega_C(y) = \Omega_C \sin(k(y - y_0))$  (see Fig. 14). Further, we couple the ground state  $|g\rangle$  to an auxiliary level  $|a\rangle$  via two moving waves with Rabi frequencies  $\Omega_1 \exp(i(\mathbf{k}_1 \cdot \mathbf{r} - \omega_1 t))$  and  $\Omega_2 \exp(i(\mathbf{k}_2 \cdot \mathbf{r} - \omega_2 t))$  incident in the  $x$ - $y$ -plane. Choosing a large detuning  $|\Delta_{AC}| \gg |\Omega_{1,2}|$ , we inevitably introduce a similar off-resonant coupling of  $|g'\rangle$  and  $|e\rangle$  with possibly slightly different Rabi frequency amplitudes  $\Omega'_{1,2}$  and detuning  $|\Delta'_{AC}| \gg |\Omega'_{1,2}|$ . Adiabatic elimination of both transitions leads to AC-Stark shifts of the ground states  $|g\rangle$  and  $|g'\rangle$  whose static part can be absorbed into an appropriate choice of the detunings  $\delta = \Omega' - \Omega$ ,  $\tilde{\Delta} = \Delta_\Lambda + \Omega$ . The resulting internal Hamiltonian of the  $\Lambda$ -system in a rotating frame is given by

$$H_{\text{int}}(x, y) = -\tilde{\Delta} |e\rangle \langle e| + \cos(\delta \mathbf{k} \cdot \mathbf{r} - \delta \omega t) (\Omega |g\rangle \langle g| + \Omega' |g'\rangle \langle g'|) + \frac{1}{2} (\Omega_P |e\rangle \langle g| + \Omega_C(y) |e\rangle \langle g'| + \text{h.c.}) \quad (\text{C2})$$

where  $\Omega = \Omega_1 \Omega_2 / (2\Delta_{AC})$  (resp.  $\Omega' = \Omega'_1 \Omega'_2 / (2\Delta'_{AC})$ ) denote the two-photon Rabi frequencies and  $\delta \omega = \omega_1 - \omega_2$  ( $\delta \mathbf{k} = \mathbf{k}_1 - \mathbf{k}_2$ ) the two-photon detuning. For  $\Omega = \Omega' = 0$ , the  $\Lambda$ -system possesses a position dependent dark state  $|E_0(y)\rangle = \sin \alpha(y) |g\rangle - \cos \alpha(y) |g'\rangle$  where  $\tan \alpha(y) = \Omega_C(y) / \Omega_P$ . For simplicity, we consider in the following the resonant case  $\tilde{\Delta} = 0$ . Then, for  $\Omega_C, \Omega_P \gg \Omega, \Omega'$  the

dark state decouples and we find after projection with  $\mathcal{P}(y) = |D(y)\rangle \langle D(y)|$

$$\mathcal{P}(y)H_{\text{int}}(x, y)\mathcal{P}(y) = \cos(\delta\mathbf{k} \cdot \mathbf{r} - \delta\omega t) \cdot (\Omega + (\Omega' - \Omega) \cos^2 \alpha(y)) |D(y)\rangle \langle D(y)|. \quad (\text{C3})$$

Due to the position dependence of the dark state, the projection of the kinetic part contained in  $\mathcal{P}(y)H_{\text{ext}}(x, y)\mathcal{P}(y)$  is non-trivial. Assuming small kinetic energy,  $E_R/\epsilon^2, \hbar\omega_T \ll \Omega_P, \Omega_C$ , additionally introduced couplings to the bright states can be neglected [35]. However, the dark state is still subject to an additional conservative potential, the first non-adiabatic correction [35]

$$V_{na}(y) = \frac{\hbar^2}{2m} (\partial_y \alpha)^2 = E_R^2 \frac{\epsilon^2 \cos^2(k(y - y_0))}{[\epsilon^2 + \sin^2(k(y - y_0))]^2}. \quad (\text{C4})$$

This potential represents the nanoscale barrier appearing where  $\Omega_C(y) \approx 0$ , whose height  $E_R/\epsilon^2$  and width  $\epsilon/k$  is determined by the ratio of amplitudes  $\epsilon = \Omega_P/\Omega_C \ll 1$  of the Rabi frequencies constituting the  $\Lambda$ -system. Physically, the potential reflects the rapid change of the dark state identity populating the state  $|g'\rangle$  only inside the nanoscale region of width  $\epsilon/k$ . Since the second term  $\sim \cos^2 \alpha(y) = |\langle g'|D(y)\rangle|^2$  in equation (C3) results from the additional Raman coupling of  $|g'\rangle$  to  $|e\rangle$ , it accordingly contributes to any relevant hopping matrix element  $B_{nn'}$  (equation (D10)) only to order  $\mathcal{O}(\epsilon^2)$ . We neglect it to arrive at the full dark state Hamiltonian  $H(t) = H_D + H_{RM}(t)$  [equations (13) and (14)].

#### Appendix D: Floquet analysis of two coupled wires

In this Appendix, we describe the numerical and perturbative calculation of the Raman assisted tunneling amplitude in the nanoscale double wire introduced in Sec. III B. The full Hamiltonian of this system  $H(t) = H_D + H_{RM}(t)$  [equations (13) and (14)] is fundamentally characterized by its discrete time translation symmetry  $H(t) = H(t + T)$  with period  $T = 2\pi/\delta\omega$  and frequency  $\delta\omega$ . It describes a periodically driven system for which Floquet's theorem yields a representation of its time evolution operator

$$U(t, t_0) = P(t) e^{iH_F[t_0](t-t_0)}. \quad (\text{D1})$$

Here,  $P(t) = P(t+T)$  is a unitary, periodic operator with  $P(t_0) = \mathbb{1}$  and  $H_F[t_0]$  the so called Floquet Hamiltonian.  $P(t)$  describes the micromotion within a single period whereas  $H_F[t_0]$  describes the effective dynamics after full periods of the driving (starting at  $t_0$ ), the macromotion, in which we are mainly interested in [87].

Truncating the Fourier expansion of its eigenstates  $H_F[t_0]$  can be computed numerically. Concretely, we use an expansion up to frequencies of  $\pm 25\delta\omega$  and truncate

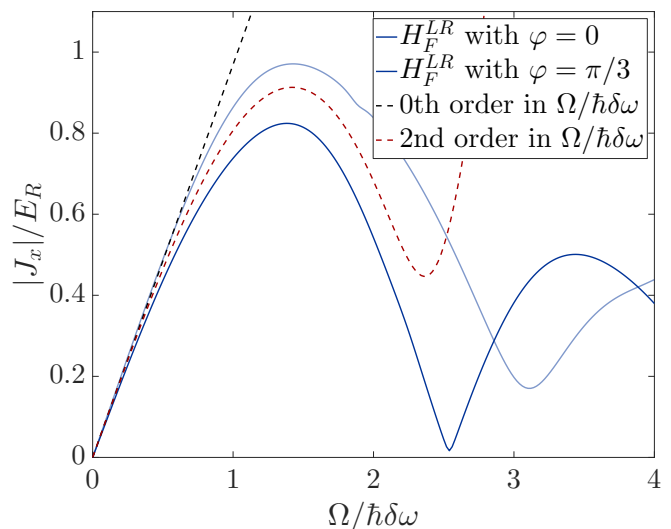


FIG. 15. (Color online) Raman induced hopping amplitude  $J = H_F^{LR}$  as a function of the two photon Rabi frequency  $\Omega$  obtained via a numerical Floquet analysis for two different initial phases (blue lines). Whereas the strong driving regime shows large phase-dependent effects, the maximal achievable coupling differs only by a few percent and is well approximated by the second order expansion (red dashed) of the manifestly phase independent effective Hamiltonian  $H_{\text{eff}}$  (see text).  $\epsilon \approx 0.1$ ,  $y_0 \approx 0.1a_H$ ,  $\delta k_y = 2k$  and  $\delta\omega \approx 1.1\Delta/\hbar$  have been chosen to maximize resonant tunneling.

the Hilbert space of the unperturbed Hamiltonian to the  $n = 15$  lowest eigenstates to calculate the effective time-averaged coupling  $J \equiv H_F^{LR}$  of left and right wire. The result is displayed in Fig. 15 (solid blue line) and shows clearly the higher order effects bounding the coupling for large driving amplitude after a linear rise in the perturbative regime (see also main text). The driving frequency  $\delta\omega$  is thereby adjusted self-consistently, such that it compensates the energy mismatch  $\Delta$  between the bare states  $|L\rangle$  and  $|R\rangle$  and static AC Stark shifts, which are caused by the periodic driving and hence depends on  $\Omega$  and  $\delta\omega$ , at the maximum of  $J$ .

So far, we considered a driving of the system starting at definite time  $t_0 = 0$  with vanishing phase at the origin (see equation (14)). However, the effect of a periodic driving and therefore  $H_F[t_0]$  typically depend on its phase at initial time [68, 70]. To quantify how these effect alter the maximal achievable coupling we include a phase  $\varphi_0$  to the Hamiltonian, i.e. replace equation (14) with

$$H_{RM}^{\varphi_0}(x, y, t) = \Omega \cos(\delta k_x x + \delta k_y y - \delta\omega t + \varphi_0). \quad (\text{D2})$$

As shown in figure 15, the coupling, i.e. the Floquet Hamiltonian  $H_F$ , depends strongly on the initial phase in the strong driving regime. However, the maximal achievable coupling varies only in the range of a few percent. To quantify this and distill the time averaged dynamics resulting purely from the periodicity of the driving, we follow an approach developed in Refs. [68, 70, 87, 88].

Via a unitary transformation, the phase dependence of  $H_F$  can be absorbed into so called kick operators  $K(t)$  yielding the representation of the time evolution operator

$$U(t, t_0) = e^{-iK(t)} e^{iH_{\text{eff}}(t-t_0)} e^{iK(t_0)} \quad (\text{D3})$$

where the effective Hamiltonian  $H_{\text{eff}}$  is by definition constant in time and independent of the phase of the driving at initial time. It captures only time averaged effects due to the periodicity of the driving. In contrast, the periodic kick operators  $K(t) = K(t+T)$  describe the micromotion within one period. For small driving  $\Omega \lesssim \hbar\delta\omega$ , a perturbative expansion in powers of  $(\Omega/\hbar\delta\omega)$  is applicable to compute  $H_{\text{eff}}$  and  $K$ . Using the Fourier decomposition

$$H(t) = H_0 + V(t) \quad (\text{D4})$$

$$V(t) = \sum_{j=1}^{\infty} V^{(j)} e^{ij\delta\omega t} + V^{(-j)} e^{-ij\delta\omega t} \quad (\text{D5})$$

with  $H_0 = \langle H(t) \rangle_{T=1/\delta\omega}$  one finds for the effective Hamiltonian [68, 88]:

$$\begin{aligned} H_{\text{eff}} = & H_0 + \frac{1}{\delta\omega} \sum_{j=1}^{\infty} \frac{1}{j} [V^{(j)}, V^{(-j)}] \\ & + \frac{1}{2\delta\omega^2} \sum_{j=1}^{\infty} \frac{1}{j^2} \left( [[V^{(j)}, H_0], V^{(-j)}] + \text{h.c.} \right) \\ & + \frac{1}{3\delta\omega^2} \sum_{j,l=1}^{\infty} \frac{1}{jl} \left( [V^{(j)}, [V^{(l)}, V^{(-l-j)}]] \right. \\ & \quad \left. - [V^{(j)}, [V^{(-l)}, V^{(l-j)}]] + \text{h.c.} \right) \\ & + \mathcal{O}\left(\frac{1}{\delta\omega^3}\right). \end{aligned} \quad (\text{D6})$$

The kick operator is given by

$$K(t) = \sum_{j \neq 0} V^{(j)} \frac{1}{i\delta\omega j} e^{ij\delta\omega t} + \mathcal{O}\left(\frac{1}{\delta\omega^2}\right). \quad (\text{D7})$$

which is first order in  $1/\delta\omega$ . Hence, initial time or phase dependent effects enter only for strong driving, as shown in figure 15. To calculate  $H_{\text{eff}}$  we move into a rotating frame defined by

$$\begin{aligned} U(t) = & e^{-i/2[(\Delta/\hbar - \delta\omega)t + \varphi_0]} |L\rangle \langle L| \\ & + e^{-i/2[(\Delta/\hbar + \delta\omega)t - \varphi_0]} |R\rangle \langle R|. \end{aligned} \quad (\text{D8})$$

For our concrete setup, only the first  $V^{(j=\pm 1)}$  and second  $V^{(j=\pm 2)}$  harmonics of the potential are non-vanishing. We find the effective Hamiltonian  $H_{\text{eff}}$  to second order in  $\Omega/\hbar\delta\omega$  in the basis spanned by wave functions in left and

right wire  $(\Psi_L(x), \Psi_R(x))$  to be

$$\begin{aligned} H_{\text{eff}}(x) = & \sum_{n=L,R} \left[ \frac{\hbar^2}{2m} \left( -i\partial_x + \frac{\Omega^2}{(\hbar\delta\omega)^2} A_n^{(2)} \right)^2 \right. \\ & \left. + \left( \frac{\sigma_n}{2} (\hbar\delta\omega - \Delta) + \frac{\Omega}{\hbar\delta\omega} \epsilon_n^{(1)} + \frac{\Omega^2}{(\hbar\delta\omega)^2} \epsilon_n^{(2)} \right) \right] |n\rangle \langle n| \\ & + e^{-i\delta k_x x} \left[ \kappa^{(0)} + \frac{\Omega^2}{(\hbar\delta\omega)^2} \kappa^{(2)} \right] |L\rangle \langle R| + \text{h.c.} \\ & + \mathcal{O}\left(\frac{\Omega^4}{(\hbar\delta\omega)^3}\right) \end{aligned} \quad (\text{D9})$$

where  $\sigma_L \equiv 1$  and  $\sigma_R \equiv -1$ . With the hopping matrix elements  $B_{nn'}$

$$B_{nn'} \equiv \langle n | e^{-i\delta k_x \hat{y}} | n' \rangle, \quad (\text{D10})$$

we have obtained a constant second order gauge potential

$$\frac{\Omega^2}{(\hbar\delta\omega)^2} A_n^{(2)} = \sigma_n \frac{\Omega^2}{(\hbar\delta\omega)^2} \frac{|B_{LR}|^2}{32} \delta k_y, \quad (\text{D11})$$

AC stark shifts of the individual levels

$$\begin{aligned} \frac{\Omega}{\hbar\delta\omega} \epsilon_n^{(1)} = & -\sigma_n \frac{\Omega^2}{\hbar\delta\omega} \frac{|B_{LR}|^2}{8}, \\ \frac{\Omega^2}{(\hbar\delta\omega)^2} \epsilon_n^{(2)} = & \frac{\Omega^2}{(\hbar\delta\omega)^2} \left[ \left( \frac{|B_{nn}|^2}{4} + \frac{1}{32} |B_{LR}|^2 \right) \frac{\hbar^2 \delta k_y^2}{2m} \right. \\ & \left. - \sigma_n \frac{|B_{LR}|^2}{16} (\hbar\delta\omega - \Delta) \right], \end{aligned} \quad (\text{D12})$$

and the Raman induced couplings

$$\begin{aligned} \kappa^{(0)} = & \Omega \frac{B_{LR}}{2}, \\ \frac{\Omega^2}{(\hbar\delta\omega)^2} \kappa^{(2)} = & -\frac{\Omega^3}{(\hbar\delta\omega)^2} \left( \frac{B_{LR}}{8} |B_{LL} - B_{RR}|^2 \right. \\ & \left. - \frac{B_{10}^*}{16} (B_{LL} - B_{RR})^2 + \frac{B_{LR}}{32} |B_{LR}|^2 \right). \end{aligned} \quad (\text{D13})$$

The absolute value of the coupling  $J = H_{\text{eff}}^{01} = e^{-i\delta k_x x} \left[ \kappa^{(0)} + \frac{\Omega^2}{(\hbar\delta\omega)^2} \kappa^{(2)} \right]$  is shown to zeroth and second order in  $\Omega/\hbar\delta\omega$  in Fig. 15. The bounding effect of the higher order processes which involve on-site and multiple intersite hopping processes is clearly visible. The driving frequency has been chosen to obtain resonant tunneling at the maximal amplitude, i.e. such the Stark shifts  $\epsilon_1$  and  $\epsilon_2$  are canceled when  $\Omega$  is chosen to maximize  $J$ . Note that the initial phase  $\varphi_0$  does not enter the effective Hamiltonian  $H_{\text{eff}}$ . In contrast, the kick operator depends explicitly on  $\varphi_0$  and is given by

$$\begin{aligned} K(t, x) = & \sum_{n=L,R} \frac{\Omega}{2i\hbar\delta\omega} e^{i(\delta\omega t - \delta k_x x - \varphi_0)} B_{nm} |n\rangle \langle n| + \text{h.c.} \\ & + \frac{\Omega}{4i\hbar\delta\omega} e^{i(2\delta\omega t - \delta k_x x - 2\varphi_0)} B_{RL} |R\rangle \langle L| + \text{h.c.} \\ & + \mathcal{O}\left(\frac{\Omega^2}{(\hbar\delta\omega)^2}\right). \end{aligned} \quad (\text{D14})$$

It leads to phase dependent effects of order  $\Omega/\hbar\delta\omega$ . To conclude, we compare our result (D9) to an approach presented in Ref. [13]. Here, a non-perturbative resummation of on-site hopping processes mediated by the matrix elements  $B_{nn}$  was performed via a transformation to another rotating frame. Time-averaging in this frame yields the well-known Bessel function renormalization of

the coupling, keeps however only terms linear in  $B_{LR}$ . In our case, all matrix elements  $B_{nn'}$  are of order unity. Hence, a selective resummation of on-site processes does not improve the agreement to the non-perturbative numerical analysis. On the contrary, the inclusion of the last term in (D13), neglected in Ref. [13], leads in our case to a better agreement of the second order perturbation theory than the partially resummed result of Ref. [13].

- 
- [1] I. Bloch, J. Dalibard, and W. Zwerger, Many-body physics with ultracold gases, *Rev. Mod. Phys.* **80**, 885 (2008).
- [2] M. Lewenstein, A. Sanpera, and V. Ahufinger, *Ultracold Atoms in Optical Lattices: Simulating quantum many-body systems* (Oxford University Press, 2012).
- [3] N. Goldman, J. C. Budich, and P. Zoller, *Nature Phys.* **12**, 639 (2016).
- [4] D. Jaksch and P. Zoller, Creation of effective magnetic fields in optical lattices: the Hofstadter butterfly for cold neutral atoms, *New Journal of Physics* **5**, 56 (2003).
- [5] S.-L. Zhu, H. Fu, C.-J. Wu, S.-C. Zhang, and L.-M. Duan, *Phys. Rev. Lett.* **97**, Spin Hall Effects for Cold Atoms in a Light-Induced Gauge Potential, 240401 (2006).
- [6] F. Gerbier, J. Dalibard, Gauge fields for ultracold atoms in optical superlattices, *New J. Phys.* **12**, 033007 (2010).
- [7] J. Dalibard, F. Gerbier, G. Juzeliunas, P. Öhberg, Colloquium: Artificial gauge potentials for neutral atoms, *Rev. Mod. Phys.* **83**, 1523 (2011).
- [8] N. R. Cooper, Optical flux lattices for ultracold atomic gases, *Phys. Rev. Lett.* **106**, 175301 (2011).
- [9] N. R. Cooper and J. Dalibard, Reaching fractional quantum Hall states with optical flux lattices, *Phys. Rev. Lett.* **110**, 185301 (2013).
- [10] N. Goldman, G. Juzeliunas, P. Öhberg, I. B. Spielman, Light-induced gauge fields for ultracold atoms, *Rep. Prog. Phys.* **77** 126401 (2014).
- [11] M. Aidelsburger, M. Atala, S. Nascimbene, S. Trotzky, Y.-A. Chen, I. Bloch, Experimental Realization of Strong Effective Magnetic Fields in an Optical Lattice, *Phys. Rev. Lett.* **107**, 255301 (2011).
- [12] J. Struck, C. Ölschläger, M. Weinberg, P. Hauke, J. Simonet, A. Eckardt, M. Lewenstein, K. Sengstock, and P. Windpassinger, Tunable Gauge Potential for Neutral and Spinless Particles in Driven Optical Lattices, *Phys. Rev. Lett.* **108**, 225304 (2012). J. Struck, M. Weinberg, C. Ölschläger, P. Windpassinger, J. Simonet, K. Sengstock, R. Höppner, P. Hauke, A. Eckardt, M. Lewenstein, and L. Mathey, Engineering Ising-XY spin-models in a triangular lattice using tunable artificial gauge fields, *Nat. Phys.*, **9**, 738 (2013).
- [13] H. Miyake, G. A. Siviloglou, C. J. Kennedy, W. C. Burton, and W. Ketterle, Realizing the Harper Hamiltonian with Laser-Assisted Tunneling in Optical Lattices, *Phys. Rev. Lett.* **111**, 185302 (2013).
- [14] M. Aidelsburger, M. Atala, M. Lohse, J. T. Barreiro, B. Paredes, and I. Bloch, Realization of the Hofstadter Hamiltonian with Ultracold Atoms in Optical Lattices, *Phys. Rev. Lett.* **111**, 185301 (2013).
- [15] M. Atala, M. Aidelsburger, M. Lohse, J. T. Barreiro, B. Paredes, and I. Bloch, Observation of chiral currents with ultracold atoms in bosonic ladders, *Nat. Phys.* **10**, 588 (2014).
- [16] M. Aidelsburger, M. Lohse, C. Schweizer, M. Atala, J. T. Barreiro, S. Nascimbène, N. R. Cooper, I. Bloch, N. Goldman, Measuring the Chern number of Hofstadter bands with ultracold bosonic atoms, *Nat. Phys.* **11**, 162 (2015).
- [17] V. Galitski and I. B. Spielman. Spin-orbit coupling in quantum gases. *Nature*, **494**, 49 (2013).
- [18] M. Z. Hasan and C. L. Kane, Colloquium: Topological insulators, *Rev. Mod. Phys.* **82**, 3045 (2010).
- [19] X.-L. Qi and S.-C. Zhang, Topological insulators and superconductors, *Rev. Mod. Phys.* **83**, 1057 (2011).
- [20] D. R. Hofstadter, Energy levels and wave functions of Bloch electrons in rational and irrational magnetic fields, *Phys. Rev. B* **14**, 2239 (1976).
- [21] L. Allen, M. W. Beijersbergen, R. Spreeuw, and J. Woerdman, Orbital angular momentum of light and the transformation of Laguerre-Gaussian laser modes, *Phys. Rev. A* **45**, 8185 (1992).
- [22] L. Allen, S. M. Barnett, and M. J. Padgett, *Optical angular momentum* (CRC Press, 2003).
- [23] S. Franke-Arnold, L. Allen, M. Padgett, Advances in optical angular momentum, *Laser & Photonics Reviews* **2**, 299 (2008).
- [24] D. C. Tsui, H. L. Stormer, and A. C. Gossard, Two-dimensional magnetotransport in the extreme quantum limit, *Phys. Rev. Lett.* **48**, 1559 (1982).
- [25] R. B. Laughlin, Anomalous quantum Hall effect: an incompressible quantum fluid with fractionally charged excitations, *Phys. Rev. Lett.* **50**, 1395 (1983).
- [26] R. Prange and S. Girvin, *The Quantum Hall Effect* (Springer, 1990).
- [27] C. L. Kane, R. Mukhopadhyay, T. C. Lubensky, The Fractional Quantum Hall effect in an Array of Quantum Wires, *Phys. Rev. Lett.* **88**, 036401 (2002)
- [28] J. C. Y. Teo and C. L. Kane, From Luttinger liquid to non-Abelian quantum Hall states, *Phys. Rev. B* **89**, 085101 (2014).
- [29] D. Bauer, T. S. Jackson, R. Roy, Quantum geometry and stability of the fractional quantum Hall effect in the Hofstadter model, arXiv:1504.07185 (2015).
- [30] E. Orignac and T. Giamarchi. Meissner effect in a bosonic ladder. *Phys. Rev. B*, **64**, 144515, (2001).
- [31] Dario Hügél and Belén Paredes. Chiral ladders and the edges of quantum Hall insulators. *Phys. Rev. A*, **89**, 023619, (2014).
- [32] M. Mancini, G. Pagano, G. Cappellini, L. Livi, M. Rider, J. Catani, C. Sias, P. Zoller, M. Inguscio, M. Dalmonte, and L. Fallani. Observation of chiral edge states with neutral fermions in synthetic Hall ribbons. *Science*, **80**

- 349, 6255, (2015).
- [33] M. Piraud, F. Heidrich-Meisner, I. P. McCulloch, S. Greschner, T. Vekua, and U. Schollwöck. Vortex and Meissner phases of strongly interacting bosons on a two-leg ladder. *Phys. Rev. B*, **91**, 140406, (2015).
- [34] Ran Wei and Erich J. Mueller. Theory of bosons in two-leg ladders with large magnetic fields. *Phys. Rev. A*, **89**, 063617, (2014).
- [35] M. Łącki, M. A. Baranov, H. Pichler, and P. Zoller, Nanoscale "Dark State" Optical Potentials for Cold Atoms, *Phys. Rev. Lett.* **117**, 233001, (2016).
- [36] F. Jendrzejewski, S. Eckel, T. G. Tiecke, G. Juzeliūnas, G. K. Campbell, Liang Jiang, and A. V. Gorshkov. Subwavelength-width optical tunnel junctions for ultracold atoms. *Phys. Rev. A*, **106** 063422 (2016).
- [37] D. Thouless, M. Kohmoto, M. P. Nightingale, and M. den Nijs, Quantized Hall conductance in a two-dimensional periodic potential, *Phys. Rev. Lett.*, **49**, 405 (1982).
- [38] R. B. Laughlin, Quantized Hall conductivity in two dimensions, *Phys. Rev. B* **23**, 5632(R) (1981).
- [39] K. C. Wright, R. B. Blakestad, C. J. Lobb, W. D. Phillips, and G. K. Campbell, Threshold for creating excitations in a stirred superfluid ring, *Phys. Rev. A* **88**, 063633, (2013).
- [40] C. Ryu, M. F. Andersen, P. Cladé, Vasant Natarajan, K. Helmerson, and W. D. Phillips, Observation of Persistent Flow of a Bose-Einstein Condensate in a Toroidal Trap, *Phys. Rev. Lett.* **99**, 260401, (2007).
- [41] M. Łącki, H. Pichler, A. Sterdyniak, A. Lyras, V. E. Lembessis, O. Al-Dossary, J. C. Budich, P. Zoller, Quantum Hall physics with cold atoms in cylindrical optical lattices, *Phys. Rev. A*, **93**, 013604, (2016).
- [42] S Hofferberth, I Lesanovsky, B Fischer, J Verdu, and J. Schmiedmayer. Radiofrequency-dressed-state potentials for neutral atoms. *Nat. Phys.*, **2**, 710, (2006).
- [43] T Schumm, P. Krüger, S Hofferberth, I. Lesanovsky, S Wildermuth, S Groth, I Bar-Joseph, L M Andersson, and J Schmiedmayer. A double well interferometer on an atom chip. *Quantum Inf. Process.*, **5**, 537, (2006).
- [44] I. M. Lifshitz. Anomalies of electron characteristics of a metal in the high pressure region. *Sov. Phys. JETP*, **11**, 1130, (1960).
- [45] In Fig. 3, we assume temperatures  $k_B T/J = 0.1$  and  $k_B T/J = 0.5$ . These are realistic experimental values in ultracold fermionic gas consisting out of  $^{40}\text{K}$  with temperature  $T = 10$  nK in an optical lattice with period  $\lambda/2 = 385$  nm [89]. The hopping amplitudes are taken to be  $J = 0.25E_R$  in the subwavelength double wire and  $J = 0.05E_R$  in the standard setup with wire separation  $\lambda/2$ .
- [46] N. R. Cooper, N. K. Wilkin, and J. M. F. Gunn, Quantum phases of vortices in rotating Bose-Einstein condensates, *Phys. Rev. Lett.* **87**, 120405 (2001).
- [47] N. Regnault and T. Jolicoeur, Quantum Hall fractions in ultracold fermionic vapors, *Phys. Rev. B* **70**, 241307 (2004).
- [48] M. A. Baranov, K. Osterloh, and M. Lewenstein, Fractional Quantum Hall States in Ultracold Rapidly Rotating Dipolar Fermi Gases, *Phys. Rev. Lett.* **94**, 070404 (2005).
- [49] A. S. Sørensen, E. Demler, and M. D. Lukin, Fractional quantum Hall states of atoms in optical lattices, *Phys. Rev. Lett.* **94**, 086803 (2005).
- [50] M. Hafezi, A. S. Sørensen, E. Demler, and M. D. Lukin Fractional quantum Hall effect in optical lattices, *Phys. Rev. A* **76**, 023613 (2007).
- [51] A. Sterdyniak, B. A. Bernevig, N. R. Cooper, and N. Regnault, Interacting bosons in topological optical flux lattices, *Phys. Rev. B* **91**, 035115 (2015).
- [52] Fractional Quantum Hall States at Zero Magnetic Field, T. Neupert, L. Santos, C. Chamon, and C. Mudry, *Phys. Rev. Lett.* **106**, 236804 (2011).
- [53] D. N. Sheng, Z.-C. Gu, K. Sun, and L. Sheng, Fractional quantum Hall effect in the absence of Landau levels, *Nat. Commun.* **2**, 389 (2011).
- [54] N. Regnault and B. A. Bernevig, Fractional Chern Insulator, *Phys. Rev. X* **1**, 021014 (2011).
- [55] N. R. Cooper, Rapidly rotating atomic gases, *Adv. Phys.* **57**, 539 (2008).
- [56] Emil J. Bergholtz and Zhao Liu. Topological flat bands models and fractional Chern insulators. *Int. J. Mod. Phys. B*, **27**, 1330017, (2013).
- [57] S. A. Parameswaran, R. Roy, and S. L. Sondhi, Fractional quantum Hall physics in topological flat bands, *Comptes Rendus Physique*, **14**, 816-839 (2013).
- [58] E. Kapit and E. Mueller, Exact Parent Hamiltonian for the Quantum Hall States in a Lattice, *Phys. Rev. Lett.* **105**, 215303 (2010).
- [59] F. D. M. Haldane, Many-Particle Translational Symmetries of Two-Dimensional Electrons at Rational Landau-Level Filling, *Phys. Rev. Lett.* **55**, 2095 (1985).
- [60] H. Li and F. D. M. Haldane, Entanglement Spectrum as a Generalization of Entanglement Entropy: Identification of Topological Order in Non-Abelian Fractional Quantum Hall Effect States, *Phys. Rev. Lett.* **101**, 010504 (2008).
- [61] A. Sterdyniak, N. Regnault, and B. A. Bernevig, Extracting Excitations from Model State Entanglement, *Phys. Rev. Lett.* **106**, 100405 (2011).
- [62] F. D. M. Haldane, "Fractional statistics" in arbitrary dimensions: A generalization of the Pauli principle, *Phys. Rev. Lett.* **67**, 937 (1991)
- [63] A. Fayyazuddin and D. Li, Haldane's Fractional Statistics and the Lowest Landau Level on a Torus, *Phys. Rev. Lett.* **76**, 1707 (1996).
- [64] B. A. Bernevig and N. Regnault, ArXiv e-prints (2012), arXiv:1204.5682 [cond-mat.str-el].
- [65] D. Jaksch, C. Bruder, J. I. Cirac, C. W. Gardiner, and P. Zoller, Cold Bosonic Atoms in Optical Lattices, *Phys. Rev. Lett.* **81**, 3108 (1998).
- [66] Q. Sun, J. Hu, L. Wen, W.-M. Liu, G. Juzeliūnas, and A.-C. Ji, Ground states of a Bose-Einstein Condensate in a one-dimensional laser-assisted optical lattice, *Scientific Reports* **6**, 37679 (2016).
- [67] C. E. Creffield, F. Sols, D. Ciampini, O. Morsch, and E. Arimondo, Expansion of matter waves in static and driven periodic potentials, *Phys. Rev. A* **82**, 035601 (2010).
- [68] N. Goldman and J. Dalibard, Periodically driven quantum systems: effective Hamiltonians and engineered gauge fields, *Phys. Rev. X*, **4**, 031027, (2014).
- [69] A magnetic length  $l_B \gg \lambda/2$  could be obtained with a high-order multiphoton Raman process.
- [70] N. Goldman, J. Dalibard, M. Aidelsburger, and N. R. Cooper. Periodically driven quantum matter: The case of resonant modulations. *Phys. Rev. A.*, **91**, 033632, (2015).
- [71] R. Fickler, R. Lapkiewicz, W. N. Plick, M. Krenn, C. Schaeff, S. Ramelow, A. Zeilinger, Quantum entangle-

- ment of high angular momenta, *Science* **338**, 640 (2012).
- [72] D. L. Andrews, *Structured light and its applications: An introduction to phase-structured beams and nanoscale optical forces* (Academic Press, 2011).
- [73] D. L. Andrews and M. Babiker, *The angular momentum of light* (Cambridge University Press, 2012).
- [74] M. Thirugnanasambandam, Y. Senatsky, K. Ueda, *Laser Physics Letters*, Generation of very-high order Laguerre-Gaussian modes in Yb: YAG ceramic laser, **7**, 637 (2010).
- [75] Y. Senatsky, J. Bisson, J. Li, A. Shirakawa, M. Thirugnanasambandam, and K. Ueda, Laguerre-Gaussian modes selection in diode-pumped solid-state lasers, *Optical review*, **19**, 201-221 (2012).
- [76] P. Zupancic, Master thesis, Harvard University (2013).
- [77] P. Preiss, R. Ma, M. E. Tai, A. Lukin, M. Rispoli, P. Zupancic, Y. Lahini, R. Islam, and M. Greiner, Strongly correlated quantum walks in optical lattices, *Science*, **6227**, 1229-1233 (2015).
- [78] F. Gerbier and J. Dalibard, Gauge fields for ultracold atoms in optical superlattices, *New J. Phys.* **12** 033007, (2010).
- [79] W. Yi, A. J. Daley, G. Pupillo and P. Zoller, State-dependent, addressable subwavelength lattices with cold atoms, *New J. Phys.* **10** 073015, (2008)
- [80] Noomen Belmechri, Leonid Förster, Wolfgang Alt, Artur Widera, Dieter Meschede and Andrea Alberti, *J. Phys. B: At. Mol. Opt. Phys.* **46** 104006, (2013)
- [81] A. Celi, P. Massignan, J. Ruseckas, N. Goldman, I. B. Spielman, G. Juzeliunas, M. Lewenstein, Synthetic gauge fields in synthetic dimensions, *Phys. Rev. Lett.* **112**, 043001 (2014).
- [82] H. M. Price, T. Ozawa, N. Goldman, Synthetic Dimensions for Cold Atoms from Shaking a Harmonic Trap, arXiv:1605.09310 (2016).
- [83] T. Y. Saito, S. Furukawa, Devil's staircases in synthetic dimensions and gauge fields, arXiv:1612.00233 (2016).
- [84] T. Ozawa and I. Carusotto, Synthetic Dimensions with Magnetic Fields and Local Interactions in Photonic Lattices, *Phys. Rev. Lett.* **118**, 013601 (2017).
- [85] C. Weitenberg, Ma. Endres, J. F. Sherson, M. Cheneau, P. Schauß, T. Fukuhara, I. Bloch and S. Kuhr, Single-spin addressing in an atomic Mott insulator *Nature* **471**, 319–324 (2011).
- [86] M. Lu, S. H. Youn, and B. L. Lev *Phys. Rev. Lett.* **104**, 063001 (2010); K. Aikawa, S. Baier, A. Frisch, M. Mark, C. Ravensbergen and F. Ferlaino, *Science* **345**, 1484 (2014), and references cited.
- [87] A. Eckardt. Atomic quantum gases in periodically driven optical lattices. arXiv:1606.08041, (2016).
- [88] A. Eckardt and E. Anisimovas. High-frequency approximation for periodically driven quantum systems from a Floquet-space perspective. *New J. Phys.*, **17**, 093039, (2015).
- [89] M. Inguscio, W. Ketterle, and C. Salomon, *Gas Di Fermi Ultrafreddi*, vol. 164 (IOS Press, 2007).